Kelvin Probe Force Microscopy in Bionanotechnology: Current Advances and Future Perspectives

Rahimi, E.; Palacios-Corella, Mario ; Mol, J.M.C.; Pané, Salvador; Puigmartí-Luis, Josep

DOI
10.1002/adma.202510671

Publication date
2025

Document Version
Final published version

Published in
Advanced Materials

ADVANCED MATERIALS
www.advmat.de

Kelvin Probe Force Microscopy in Bionanotechnology: Current Advances and Future Perspectives

Ehsan Rahimi, Mario Palacios-Corella, Arjan Mol, Salvador Pané,* and Josep Puigmartí-Luis**

Kelvin probe force microscopy (KPFM) is a highly advanced technique offering notable surface sensitivity and high lateral resolution, ranging from micrometres to the sub-nanometre scale. This scanning probe technique effectively detects local electrical surface potential (ESP), influenced charge distribution, and work function differences, making it essential for studying biological and biochemical processes, from single molecules to complex cellular structures. By enabling nanometre-resolution analysis under simulated conditions, KPFM provides crucial insights into the physicochemical evolution, functionality, and structural organization of biomolecular systems. Recent advancements have significantly expanded KPFM's capabilities, revealing ESP characteristics in diverse biological entities, including single proteins, DNA strands, lipid films, fibrils, and complex neuronal structures. The technique also facilitates the study of biomolecular nanolayers on advanced nanomaterials like gold nanoparticles and carbon nanotubes, enhancing its role in bio-nanotechnology. Such versatility highlights KPFM's transformative potential in elucidating biomolecular interactions at unprecedented resolutions. This review critically analyses recent advancements, addresses ongoing challenges in measuring ESP in biological samples, and highlights emerging strategies to improve resolution and sensitivity. Additionally, KPFM's implications in diagnostics, biosensing, tissue engineering, therapeutics, drug screening, and Alzheimer's research are explored, establishing it as a powerful tool at the intersection of nanotechnology and biomedical innovation.

1. Introduction

From single molecules to entire tissues, electrical properties significantly influence the structural integrity and functionality of biological systems.[1,2] Far from being mere byproducts of nature, these properties actively shape biological structures, mediate cellular interactions, and drive essential processes like enzymatic catalysis, signal transduction, respiration, and metabolism.[3–6] In the quest for a deeper understanding of biological systems, detecting and analyzing these electrical responses can provide invaluable insights, unlocking new perspectives on a wide range of biological processes.

Accordingly, Kelvin probe force microscopy (KPFM) stands out as a highly surface-sensitive technique for studying surface electronic properties such as electrical surface potential (ESP) distributions in biological materials, as well as local work function changes in functionalized bio-interfaces. With high lateral resolution, ranging from the micrometer[7] to nanometer[8] and even angstrom[9,10] scales, KPFM enables precise mapping of these surface properties with high spatial accuracy. This sensitivity and resolution spanning different dimensions make KPFM a particularly powerful probe technique, as it can simultaneously map ESP distribution with high precision. Unlike techniques such as electrostatic force microscopy (EFM),[11–13] scanning tunneling microscopy and spectroscopy (STM/STS),[14,15] and current-sensing atomic force microscopy (CS-AFM),[16,17] which mainly rely on electron tunneling or

E. Rahimi, A. Mol
Department of Materials Science and Engineering
Delft University of Technology
Mekelweg 2, Delft 2628 CD, The Netherlands
E-mail: e.rahimi-2@tudelft.nl

The ORCID identification number(s) for the author(s) of this article can be found under https://doi.org/10.1002/adma.202510671

DOI: 10.1002/adma.202510671

M. Palacios-Corella, J. Puigmartí-Luis
Departament de Ciència dels Materials i Química Física
Institut de Química Teòrica i Computacional
Universitat de Barcelona
Barcelona 08028, Spain
E-mail: josep.puigmarti@ub.edu

S. Pané
Multi-Scale Robotics Lab
Institute of Robotics and Intelligent Systems
Department of Mechanical and Process Engineering
ETH Zurich
Tannenstrasse 3, Zurich 8092, Switzerland
E-mail: vidalp@ethz.ch

J. Puigmartí-Luis
Institució Catalana de Recerca i Estudis Avançats (ICREA)
Pg. Lluís Companys 23, Barcelona 08010, Spain

Table 1. Summary of scanning probe microscopy techniques and the main electronic properties they measure, including the principle of measurement and the role of the tip apex in each technique.

Technique	Measurement principle	Main electronic properties measured	Notes
STM/STS	Measures tunneling current between the tip and the sample	Local density of states; electronic structure	High spatial resolution; requires conductive or semi-conductive samples
EFM	Measures electrostatic forces between the tip and the sample	Electrostatic forces; relative surface charge distribution	Non-contact; sensitive to charge density variations
CS-AFM	Measures current flow through the tip in contact with the sample	Local current (conductivity mapping)	Requires physical contact; provides local I-V curves
KPFM	Establishes and measures electrostatic forces to determine the contact potential difference (CPD) between the tip and the sample	Surface potential or work function difference	Non-contact; directly measures CPD or work function variations

current measurements, KPFM offers direct insight into electrostatic properties without perturbing the sample surface. **Table 1** provides a concise comparison among these techniques, emphasizing their different measurement principles and the unique capabilities of KPFM.

Additionally, its high sensitivity makes KPFM especially suitable for investigating organic materials[18,19] while its precision and minimally invasive nature enable detailed studies of biological and chemical systems in biophysics and biomedical surface science.[20–22] Moreover, KPFM offers unparalleled advantages for various advancements in bionanotechnology, including diagnostics,[23,24] biosensing,[25,26] tissue engineering,[27,28] therapeutics,[29] drug screening,[23,30] and Alzheimer's research.[31] Its ability to directly detect single molecules with high spatial resolution, combined with its capacity to provide detailed insights into molecular interactions at the nanoscale in a label-free manner, positions KPFM-based nano/biodiagnostic systems as a cutting-edge alternative to traditional bioassays.[32,33] These capabilities enable highly sensitive, non-invasive, and precise characterization essential for early diagnosis and personalized treatments.

This review article explores recent advances in the application of KPFM for analyzing ESP in biological systems across nano- to microscale dimensions. The discussion is structured to highlight the role of KPFM in progressively more complex biological systems, providing a comprehensive overview from simple biomolecules to intricate cellular assemblies. The topics covered include the characterization of proteins, fibrils, lipids, DNA, and cells—systems that are central to advancements in therapeutics, drug screening, tissue engineering, Alzheimer's disease research, and nano-biosensing technologies, as schematically depicted in **Figure 1**. Before examining the role of KPFM in each of these biological contexts, we first outline the fundamental principles of the technique, explaining how KPFM captures ESP distribution and emphasizing recent developments across fields in high-resolution probing.

2. KPFM's Principles and Recent Advances in High-Resolution Probing

The use of scanning probe microscopy to measure ESP at high spatial resolution was first demonstrated by Weaver et al. (January 1991),[34] who developed a vibrating probe technique based on AFM to map electrostatic potential. Their work laid the conceptual groundwork for later developments in nanoscale surface potential mapping. Shortly thereafter, Nonnenmacher et al. (April 1991)[35] extended these ideas, introducing what is now known as KPFM. Since then, KPFM has become an essential characterization tool, especially as electronic materials have scaled down and low-dimensional systems have gained prominence.[36] Unlike standard AFM, KPFM measures the local contact potential difference (ΔCPD) between a conductive AFM tip and the sample surface.[37] This enables high-resolution imaging of the ESP or work function (Φ),[20,38,39] providing insights into charge distribution, doping variations, and electronic properties at the nanoscale.

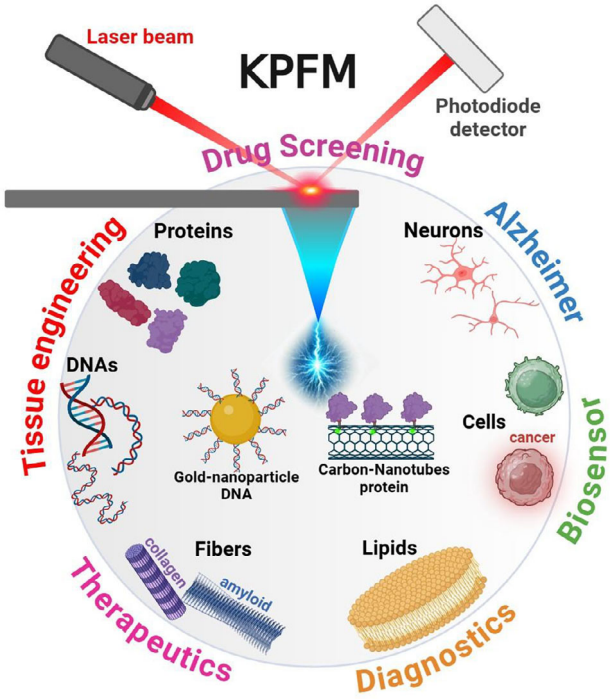

Figure 1. Schematic representation of KPFM application in bionanotechnology. A diverse range of micro- and nanoscale biological entities have been characterized, including single proteins, protein thin films, single DNA strands, DNA thin films, lipid films, cells, and neuronal structures. Notably, KPFM has been used to analyze nanolayers of proteins and DNA functionalized on gold nanoparticles and carbon nanotubes.

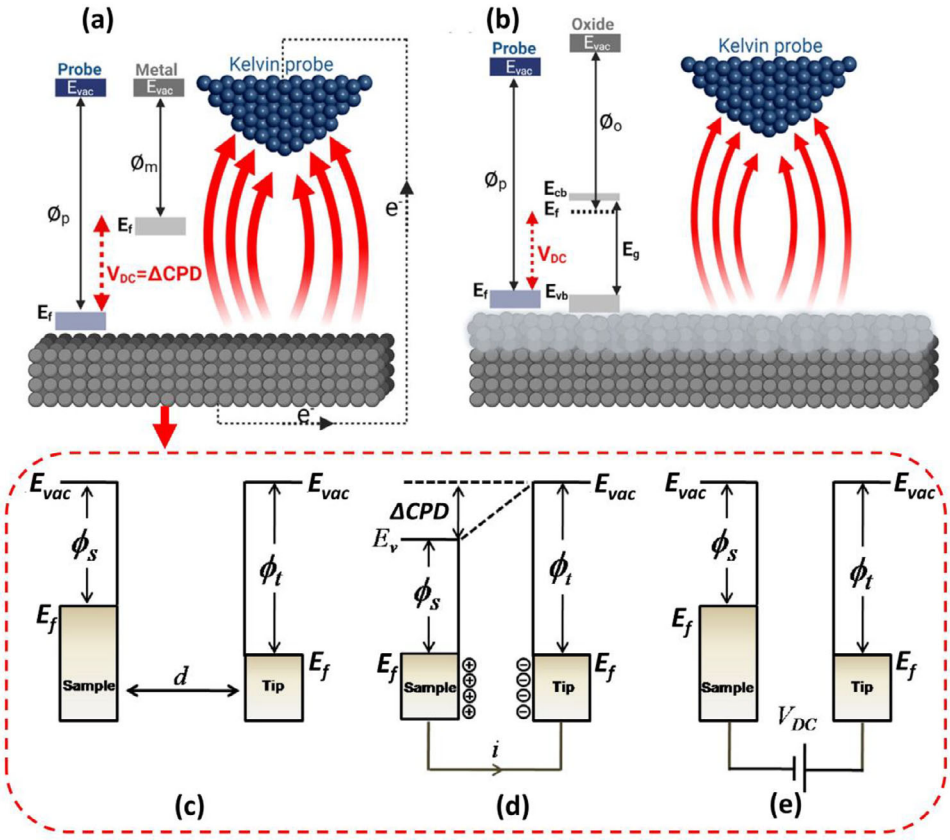

Figure 2. A schematic depiction of the KPFM principle, accompanied by an energy level diagram, illustrates the electrostatic interaction at the atomic scale between a conductive AFM tip apex and a) metallic or b) semiconductor oxide bulk materials. Adapted with permission.[40] Copyright 2022, American Chemical Society. The electronic energy levels of the sample and AFM tip are described for three distinct conditions: c) the tip and sample are separated by a distance *d*, with no electrical interaction, d) the tip and sample establish electrical contact, and e) an external bias (V_{DC}) is applied between the tip and sample to compensate for the contact potential difference (ΔCPD) and eliminate the resulting electrical force. The vacuum energy and Fermi energy levels are denoted as E_{vac} and E_f, respectively. Adapted with permission.[38] Copyright 2011, Elsevier.

The principles underlying KPFM are depicted in **Figure 2**, which includes energy diagrams illustrating the interaction between the AFM tip apex and the sample surface, either a metal (Figure 2a) or an oxide film/metal interface modeled as an n-type semiconductor (Figure 2b). These diagrams show critical energy parameters, valence band (E_{vb}), conduction band (E_{cb}), Fermi level (E_f), bandgap energy (E_g), and vacuum level (E_{vac}),[40] which helps elucidate the electronic structure of the studied materials. Mechanistically, during KPFM measurements, a bias voltage (V_{DC}) is applied while maintaining a fixed tip–sample distance (Figure 2c). The resulting ΔCPD (Figure 2d) reflects the work function difference between the probe (Φ_p) and the sample surface (Φ_s). This relationship is governed by the following equation:

$$\Delta\mathrm{CPD} = \frac{(\phi_p - \phi_s)}{-e} \tag{1}$$

here, *e* denotes the elementary charge. To nullify the electrostatic force (F_{EF} *(z)*) during measurement, the external bias voltage is tuned such that $V_{DC} = \Delta\mathrm{CPD}$ (Figure 2a,e). This ensures accurate compensation of potential differences between the tip and sample.

The electrostatic force between the tip and surface is governed by:[38]

$$F_{EF}(Z) = -\frac{1}{2}\Delta V^2 \frac{dc\ (z)}{dz} \tag{2}$$

where *z* is the distance perpendicular to the sample surface, $\Delta V = V_{DC} - \Delta\mathrm{CPD}$, and *dC (z)/dz* represents the capacitance gradient. These electrostatic forces are categorized into two types: i) capacitive forces, affected by ESP and dielectric screening; and ii) Coulombic forces, arising from static charges and multipole interactions.[41] Together, they determine the total work function difference (Φ_{total}) measured as ΔCPD. It should be noted that in complex materials, such as metallic alloys, mixed oxide phases, or regions containing both n- and p-type semiconductors, the local ESP is governed by a concentration-weighted average of the individual work functions. This averaging effect leads to the effective Φ_{total} observed by KPFM.[42]

KPFM can operate in several modes, including amplitude-modulated (AM), frequency-modulated (FM), dual-frequency-modulated (DFM), and pulsed force (PF) techniques, each designed to overcome specific limitations in resolution, signal stability, or compatibility with soft matter and solid materials.[43,44]

Table 2. Experimental insights into the use of KPFM mode for detecting specific biological molecules, focusing on unique biomolecular interactions and broader applications in nanobiotechnology. Amplitude modulation (AM), frequency modulation (FM), Dual frequency modulation (DFM).

Mode	Tip coating	Tip radius	Tip lifting	Biological molecule/functionalization	Type of binding/detection	Potential of application	Refs.
AM-KPFM	Co/Cr	35 nm	15 nm	Protein (Avidin)	biotin and glycoprotein avidin	Biosensor	[7]
AM-KPFM	Co/Cr	35 nm	15 nm	ssDNA (15 nucleotides of anthrax/malaria)	ssDNA probe with its complement	Biosensor	[7]
AM-KPFM	Pt/Ir	20 nm	5 nm	Protein (Kinase)	Protein kinase and small ligands	Therapeutics/ drug screening	[8]
DFM-KPFM	Pt/Co	25 nm	–	Protein (Avidin) and DNA	Individual electrostatic potential of avidin and DNA	General bioscience	[45]
FM-KPFM	Cr/Pt	–	50 nm	lipid-based surfactant (BLES)	BLES and cholesterol	General bioscience	[127]
DFM-KPFM	Ag_2Ga	25 nm	4 nm	Protein (lysozyme)	Aptamer and lysozyme	Biosensor	[131]
AM-KPFM	Pt/Ir	20 nm	45 nm	DNA-capped gold nanoparticles and nucleic acids	DCNP and single nucleotide polymorphism	Bioassays	[156]
AM-KPFM	Pt/Ir	20 nm	5 nm	Protein (thrombin) and ACNT	Aptamer in CNT and thrombin	Diagnostics and drug screening	[23]
AM-KPFM	Pt/Ir	20 nm	5 nm	DNA	Ag^+ ions and DNA	Biosensor	[141]
AM-KPFM	Pt/Ir	20 nm	40 nm	PC12 cells and hippocampal neurons	Individual electrostatic potential of cell bodies and nerves	Biosensor	[31]
AM-KPFM	Pt/Ir	25 nm	50 nm	HepG2 cell	Curcumin concentrations impact on HepG2 cell	Therapeutic efficacy and drug screening	[30]
AM-KPFM	Pt/Ir	7 nm	30 nm	PC12 cells	Effect of ROS on PC12 cell's plasma membrane	Biosensor and Therapeutic efficacy	[29]
AM-KPFM	Doped Si	10 nm	20 nm	Collagen fibrils	Ionization state of type-I-collagen fibrils	Tissue engineering	[24]
AM-KPFM	Pt/Ir	20 nm	10 nm	DNA-capped	Ag^+ ions and DCNP	Biosensor	[25]
AM-KPFM	Pt/Ir	20 nm	5 nm	Kirsten rat sarcoma viral oncogene homolog (KRAS) and epidermal growth factor receptor (EGFR)	KRAS and EGFR mutation and gold nanoparticles	Diagnostics	[26]
AM-KPFM	Pt/Ir	35 nm	250 nm	Immunoglobulins (IgM, IgG)	Immunoglobulins (IgM, IgG) and their cognate antibodies (anti-IgM, anti-IgG)	Biodevice	[72]
DFM-KPFM	Doped Si	7 nm	24-47 nm	DNA	Individual electrostatic potential of DNA	Biosensor	[44]
FM-KPFM	Cr/Au	35 nm	–	lipid mixtures	Nanodomains in complex lipid mixtures	General bioscience	[132]
FM-KPFM	Cr/Au	35 nm	–	DNA and lipid–gemini surfactant	DNA with lipid–gemini surfactant monolayers	Gene delivery	[126]
AM-KPFM	Cr/Au	35 nm	10 nm	Ocular Lipid	Individual electrostatic potential of human meibum	Ocular research	[200]
AM-KPFM	Pt/Ir	25 nm	10 nm	Amyloid-b_{42}	Individual electrostatic potential of Amyloid-b_{42}	Alzheimer's disease	[201]
FM-KPFM	Pt/Ir	25 nm	11 nm	Double stranded DNA (dsDNA)	Individual electrostatic potential of dsDNA	General bioscience	[138]
AM-KPFM	Pt/Ir	25 nm	–	Collagen fibrils	CO_3^{2-}/HCO^{3-} ions impact on the structure of collagen fibrils	Tissue engineering	[93]
AM-KPFM	Pt/Ir	20 nm	5 nm	Amyloids (β-lactoglobulin fibril)	pH impact on amyloid fibrils	Tissue engineering	[28]
AM-KPFM	Doped Si	10 nm	3 nm	Collagen fibrils	Glutaraldehyde impact on collagen fibrils	Tissue engineering	[202]
AM-KPFM	Doped Si	10 nm	0	Collagen fibrils	Glycation impact on collagen fibrils	Tissue engineering	[95]

AM-KPFM detects the electrostatic force between the tip and sample and is typically performed in lift mode to decouple topography and ESP signals.[20,40] It is widely used due to its simplicity and compatibility with soft samples, but it suffers from reduced spatial resolution and strong dependence on tip geometry and lift height, often leading to signal averaging artifacts.[43]

In contrast, FM-KPFM detects the gradient of the electrostatic force.[18] enabling superior spatial resolution (<50 nm) and higher accuracy, particularly for features larger than the tip radius.[43] FM-KPFM is less affected by lift height and topographic cross-talk, but requires more complex instrumentation and stiffer cantilevers, limiting its use with soft matter. To bridge these advantages, DFM-KPFM utilizes a single-pass technique, where topography and KPFM signal are acquired simultaneously and separately, each recorded at a different cantilever oscillation frequency.[44] DFM-KPFM offers improved signal separation, enhanced spatial fidelity, and operational stability, making it a powerful modality for nanoscale studies of complex or delicate systems.[45]

PF-KPFM is a novel KPFM modality that maps ESP during the momentary tip–sample detachment phase of peak force tapping (PFT), eliminating lift mode.[46–48] Using a field-effect transistor (FET) to switch tip-sample connectivity, Coulombic forces arising from Fermi-level alignment are amplified and measured via a feedback loop to extract CPD. Operating effectively in ambient and vacuum environments, PF-KPFM enables high-resolution (≈10 nm) and low-force measurements compatible with various soft biological materials.[46]

Regardless of measurement mode, measurement accuracy is influenced by the probe's physical and chemical characteristics, such as tip height, tip radius, and conductive coating (e.g., Pt-Ir, Co/Cr, doped silicon, etc). Tip lift height and scan frequency also critically affect the resolution and sensitivity of features, particularly in relation to surface morphology and feature size. To aid readers, **Table 2** summarizes key findings from various KPFM studies, highlighting how measurement modes, tip parameters, and scan conditions influence resolution, sensitivity, and surface interactions.

While the ability to map ESP is fundamental, KPFM can also offer key insights into electronic and chemical heterogeneities across a wide range of systems. By correlating spatial variations in local charge and potential with structural or compositional features, KPFM reveals interactions and behaviors that are otherwise inaccessible, making it particularly suited to exploring nanoscale mechanisms that govern material functionality. This unique sensitivity has led to a series of breakthroughs in both molecular and extended systems. For instance, KPFM has revealed anisotropic charge distributions such as the s-hole, a feature critical to halogen bonding and molecular interactions (**Figure 3**a–c).[9] It has also enabled direct visualization of the charge distribution in individual molecules, like carbon monoxide,[9] enhancing our understanding of molecular electrostatics. In extended systems, KPFM has probed ESP variations in monolayer hexagonal boron nitride, uncovering localized charge regions (Figure 3d).[49] Moreover, KPFM has also proven invaluable in solid-state applications. On metallic surfaces, it detects local work function variations due to surface reconstruction, adsorbates, or chemical modifications.[50] In oxides, including insulating oxides[51] and transition metal oxides,[52] KPFM enables precise mapping of local ESP distribution, which is critical for understanding the biodegradation process and biocatalytic activity, and electronic transport. Furthermore, KPFM is highly sensitive to localized charges[53] and surface states such as defects,[54] making it critical for characterizing semiconductor interfaces where charge inhomogeneities affect device performance.

KPFM also excels in band alignment studies,[55,56] a key parameter in designing semiconductor heterojunctions, organic semiconductors,[57] and layered optoelectronic materials. It plays a role in identifying charged contaminants[58] and analyzing organic layers[22,59] that can impact device performance and stability. These capabilities position KPFM as a transformative tool in the development of photovoltaic and sensing devices (Figure 3e,f),[60–62] where understanding charge distribution and dynamics is essential.

Altogether, the versatility of KPFM makes it a cornerstone technique across disciplines, from condensed matter physics to materials design. Importantly, KPFM also holds significant potential for advancing biological applications, where nanoscale insights into ESP distribution can deepen our understanding of complex biomolecular interactions. Nonetheless, several important considerations arise when applying KPFM in these contexts.

The measured ΔCPD, representing a relative rather than absolute ESP, originates from the fundamental electrostatic interactions between the conductive AFM tip and the sample. When dealing with soft and heterogeneous biological samples, however, both the implementation of KPFM and the interpretation of its results require additional nuance.[22] In such systems, ΔCPD reflects not just intrinsic material properties like the work function, but also interfacial effects caused by adsorbed molecular dipoles, localized charges, and dielectric screening.[18] For instance, when a monolayer or multilayer of biological soft matter (BSM) such as proteins or DNA is adsorbed onto a flat solid surface, the measured ΔCPD is modulated by the effective molecular dipole (μ_{BSM}), band bending (Δ_{bb}), and interfacial bond (Δ_{bond}, due to the new arrangement of electron density at the BSM/solid interface).[40] Accordingly, the resulting local surface potential of the BSM–solid interface ($SP_{BSM\text{-}solid\ surface}$) can be expressed as:[19]

$$SP_{BSM-solid\ surface} = SP_{solid\ surface} + \mu_{BSM/e} + \Delta_{bond} \quad (3)$$

It is common to observe ΔCPD responses in the range of a few to tens of millivolts when measuring BSM with KPFM. This signal typically arises from changes in molecular dipole orientation, interfacial bonding, or minor band bending at the solid surface–BSM interface.[20] While these values are small, they are significant given the ultrathin nature of BSM films and their low dielectric constant, which amplifies their influence on the total ESP. Another key consideration is that ΔCPD is not strictly localized. As Liscio et al. emphasized, the long-range nature of Coulombic interactions means that the signal is spatially averaged over an effective tip–sample interaction area, determined by the tip radius, cone angle, and cantilever geometry.[19] Consequently, when the lateral dimensions of the BSM are comparable to or smaller than this resolution (≈tens of nanometres), the measured surface potential becomes a weighted average of contributions from the BSM, underlying substrate, and surrounding materials. This multifactorial sensitivity is both an advantage and a central interpretative challenge in biological KPFM. Therefore, a rigorous interpretation of ΔCPD values must be supported by complementary experiments, theoretical modeling, and careful consideration of tip geometry and environmental conditions.

Beyond sample-induced artifacts, the measurement environment itself poses additional challenges. KPFM is predominantly applied under ambient or vacuum conditions, but biologically relevant studies typically require aqueous environments such as phosphate-buffered saline (PBS) or HEPES solutions. These media, rich in mobile ions and polar water molecules, lead to the formation of electric double layers (EDLs) that significantly attenuate measurable electrostatic forces. Moreover, they introduce parasitic oscillations and surface stress on the cantilever, complicating the reliable mapping of ESP.[63] Furthermore, the DC voltage bias used in conventional KPFM can also induce unwanted cantilever oscillations, electrochemical reactions, and even electrolysis, further impairing measurements in liquids.[64]

To address these limitations, several adapted techniques have been developed. Alternating current KPFM (AC-KPFM),

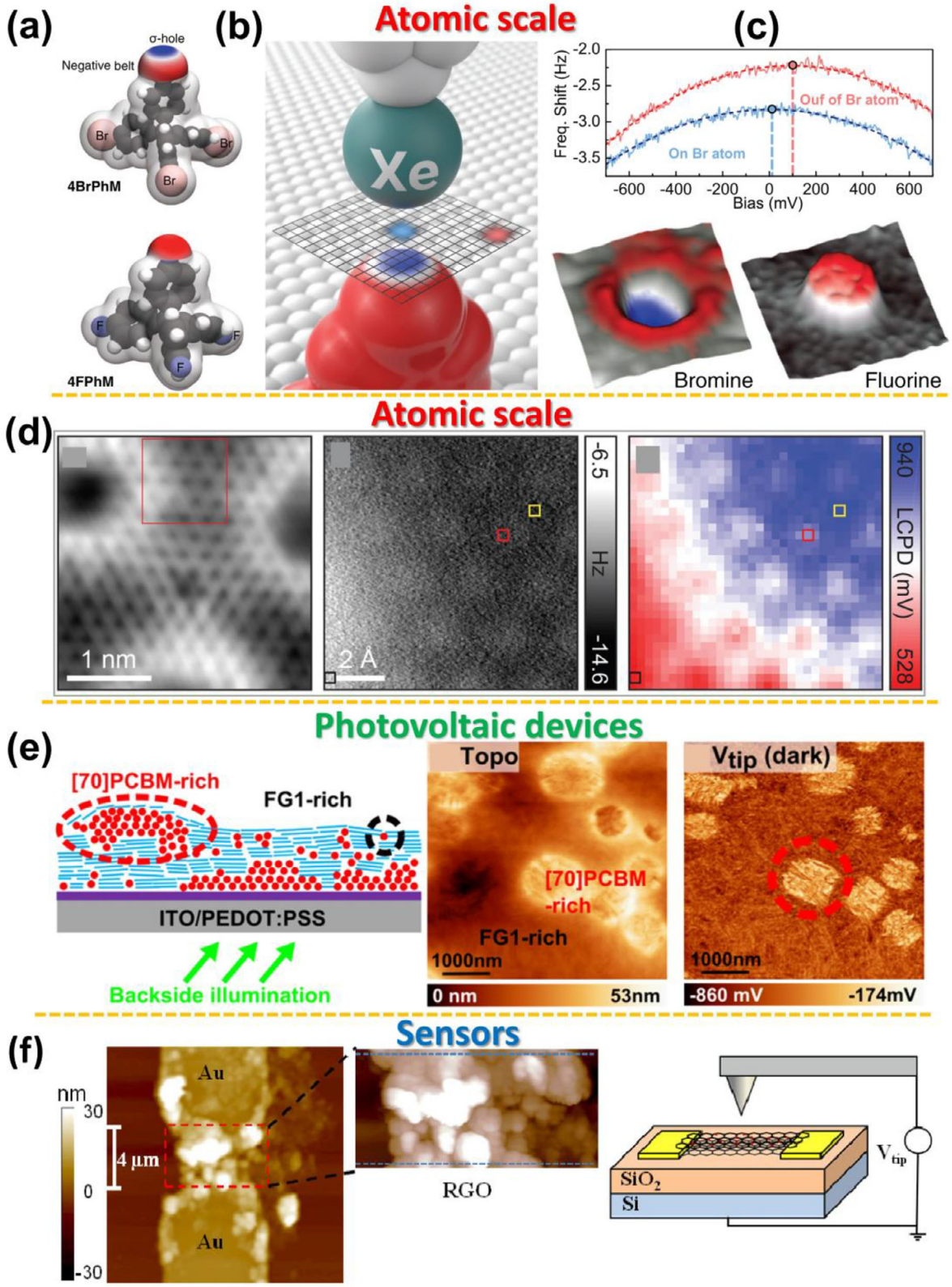

Figure 3. a) Electrostatic potential maps for the 4BrPhM and 4FPhM molecules highlight key features of their outermost Br and F atoms. The analysis shows an s-hole on the Br atom, whereas the F atom displays a uniform isotropic negative charge, b) Schematic depiction of the acquisition method using a functionalized Xe-tip across a 2D grid. c) Example $\Delta f(V)$ parabolas measured at the center (blue) and periphery (red) of the 2D grid. Vertical dashed lines mark the V_{LCPD} values derived from the parabolas, which serve as the basis for generating the 2D KPFM image, 3D rendering of KPFM images (V_{LCPD}

for instance, replaces the conventional DC bias with a high-frequency AC excitation, effectively suppressing electrochemical side effects while enabling the mapping of spatially fixed surface charges—such as ionized amino and carboxyl groups in proteins—within aqueous environments.[64] Additionally, dual-harmonic KPFM (DH-KPFM) and open-loop electric potential microscopy (OL-EPM) circumvent the feedback loop by analyzing frequency-resolved cantilever responses. These methods enhance measurement robustness, reduce drift sensitivity, and extend KPFM's applicability to biological samples, colloidal systems, and interfacial electrochemistry under native-like conditions.[65] As summarized in **Table 3**, these developments represent a critical shift from conventional, dry-state measurements toward real-time, in situ bioelectrical imaging.[66]

These methodological advances have significantly expanded the scope of KPFM in complex biological systems, enabling direct investigations of biomolecular electrostatics under near-physiological conditions. In the following sections, we explore how KPFM is applied to study ESP in increasingly complex biological systems—ranging from single proteins and DNA strands to complex neuronal structures—and examine its role in integrating biomolecules with functional nanomaterials such as gold nanoparticles (AuNPs) and carbon nanotubes (CNTs). These developments hold far-reaching implications for therapeutics, drug screening, tissue engineering, Alzheimer's disease research, and nanoscale biosensing.

3. KPFM in Protein-Based Research

3.1. Fundamental Insights into Single-Molecule Protein's ESP

Proteins, as nanoscale biological entities, are assemblies of amino acids intricately folded into specific structures that define their function and electronic properties. Recent advances in synthetic biology have enabled the design of proteins with tailored structures, allowing precise control over their molecular composition and conductivity.[67,68] This tunability is particularly crucial in bioelectronics, where proteins function as soft-conductive materials whose electrical properties are dictated by their intrinsic molecular structure, such that even subtle modifications in amino acid sequences can induce profound changes in electronic behavior. Moreover, when structured into nano-biofilms on biomaterial surfaces or bioelectronic device interfaces, proteins play a crucial role in biotechnology innovations.[69,70] Consequently, understanding the ESP, surface charge, and electrostatic forces in proteins is essential for optimizing their interactions with biological systems,[71,72] shaping key processes such as enzymatic activity,[73,74] signal transduction,[75] and immune responses.[76] This can be clearly observed in protein kinases (PKs). PKs are a diverse family of enzymes involved in the regulation of essential cellular processes, such as signal transduction, by transferring phosphate groups to target proteins.[77] One key aspect of PKs is that their mutation (inhibition) leads to a loss-of-function and is strongly associated with the onset and progression of numerous cancers.[78–80] Thus, studying PKs' molecular interactions, especially with small ligands such as adenosine-5′-triphosphate (ATP) or inhibitors, is essential to understanding their role in living organisms. However, the task presents significant challenges due to spatial resolution limitations in conventional probing techniques, which can be overcome by taking advantage of the spatial resolution of KPFM. For instance, it has been observed that exposing PKs to ATP leads to a significant negative shift in ESP, ≈-25 mV, relative to the native PK (**Figure 4**b–d). This shift was attributed to the strong negative charges of ATP after binding to the PK. However, when the PKs were exposed to a mixture of ATP and an inhibitor (Imatinib), the ESP was comparable to that of the native PK.[8] This observation suggested that Imatinib inhibits the PK activity by preventing ATP binding. Therefore, KPFM offers a powerful solution to observe ATP-driven activation of PKs and their inhibition, enabling the unambiguous detection of single ATP binding events on individual PK molecules (Figure 4a). Such a type of detection illustrates the significant capability of KPFM for investigating disease-relevant biomolecular dynamics.[33]

Ferritin is another protein that can help further illustrate the role of KPFM in enabling the fundamental understanding of proteins. Ferritin is a conserved iron-storage protein found across animals, plants, and bacteria.[81] While its function differs significantly from protein kinases, it also plays a crucial role in cellular regulation. In the human body, it is primarily localized in the liver and spleen, as well as near intercellular iron-based oxide NPs, particularly during inflammatory responses.[82] Given its role in iron regulation, ferritin interacts with therapeutic magnetic-oxide NPs, which are widely explored for biomedical applications.[83] However, the biodegradation of these NPs and their subsequent metal ion release can significantly affect apoferritin—the de-ironed ferritin—structure and function, leading to deformation and potential dysfunction.[84]

maps) obtained with an Xe-tip, resolving bromide and fluoride atoms in 4BrPhM and 4FPhM molecules. Blue areas correspond to lower V_{LCPD} values, while red areas correspond to higher ones. Adapted with permission.[9] Copyright 2021, Science. d) Scanning tunneling microscopy (STM) image of the hBN moiré. Setpoint conditions: bias voltage = 0.05 V, current = 0.30 nA. Non-contact atomic force microscopy (nc-AFM) constant-height image of the region indicated by the red square. Parameters: bias voltage = 0.05 V, current = 0.30 nA, vertical offset $\Delta z = -0.80$ Å. Concurrently recorded local contact potential difference (LCPD) map, providing atomic-scale contrast. Adapted with permission.[49] Copyright 2018, American Chemical Society. e) Diagram illustrating the proposed morphology of the oligothiophene-fluorenone oligomer (FG1): [6,6]-phenyl C70 butyric acid methyl ester ([70] PCBM) blend. Blue lines represent FG1 stacks, and red circles indicate[70] PCBM aggregates. Upon annealing, phase separation leads to mesoscopic[70] PCBM clusters, marked by red-dotted contours. A nanoscopic[70] PCBM cluster near the surface is highlighted with a black-dotted circle. Post-annealing large-scale (5000 × 5000 nm^2) topographic and KPFM potential images reveal the blend's structural and electronic characteristics. Adapted with permission.[60] Copyright 2016, American Chemical Society. f) The AFM topographic image illustrates an RGO-sensing device, featuring two Au electrodes (source and drain) and reduced graphene oxide (RGO) platelets assembled in the central region between the electrodes. The platelets have a linear size of 0.5–1 µm and a thickness of 20–50 nm, as characterized by AFM. The red dotted square highlights the region analyzed with KPFM, shown in higher resolution in the middle inset. Blue dotted lines in the inset mark the positions of the Au electrodes. A schematic of the KPFM setup shows overlapping RGO platelets positioned between the Au electrodes. Adapted with permission.[62] Copyright 2013, Institute of Physics.

Table 3. Comparison of major KPFM modalities for biological soft matter applications. The table highlights typical measured force, usage frequency and voltage, environment, resolution, and advantages specific to soft or hydrated biological materials.

KPFM mode	Force measured	Feedback mechanism	Environment	Resolution	Key advantages	Biological application
AM-KPFM	Long-range electrostatic force	DC feedback	Air/vacuum	Low–Medium	Soft sample friendly (due to soft and low-stiffness cantilevers)	Most biological soft matter (proteins, DNA, lipid bilayers, etc.)
FM-KPFM	Short-range electrostatic force gradient	DC feedback	Air/vacuum	High (<50 nm)	Less distance dependence, fewer artifacts	Less compatible with soft or hydrated biological matter
DFM-KPFM	Electrostatic force and gradient (dual modes)	DC feedback	Air/vacuum	Medium–High	Single-pass, stable in soft matter	Medium compatible with biological soft matter
PF-KPFM	Electrostatic force (via pulsed/peak force tapping, no lift mode)	Lock-in amplifier with FET switching	Air/vacuum	High (<10 nm)	No external AC voltage, single pass, fewer artifacts and distortions, reduced sample damage	Highly compatible with soft biological matter
AC-KPFM	Capacitive response to high-frequency AC field	Closed-loop, AC voltage of twice frequency (2ω)	Liquid	Medium	Avoids DC-induced unwanted redox reactions and electrokinetic effects	Real in-situ potential mapping in simulated biological environments
OL-EPM	Capacitive response to high-frequency AC bias modulation	Open-loop, frequencies of ω and 2ω	Liquid	Medium	Avoids DC-induced unwanted redox reactions and electrokinetic effects	Real in-situ potential mapping in simulated biological environments

To understand this interaction between the iron released during the biodegradation of therapeutic magnetic-oxide NPs and apoferritin, some of us have used KPFM to monitor changes in single molecules of apoferritin, filled-apoferritin molecules, and apoferritin nanofilms[20] (Figure 4e). The experimental results revealed that after a 48 h incubation in a protein and nanoparticle-containing medium, the characteristic apoferritin cavity disappeared. Simultaneously, the protein's height increased from ≈3.5 to 7.5 nm, suggesting cavity filling by NPs. Structural modifications also led to an elevation in the electronic ESP of the filled apoferritin surface from 4.2 to 6.5 mV. These compositional changes likely augmented electrostatic interactions and modulated the surface charge, alongside energy diagram shifts that intensified the protein's interaction with the conductive AFM tip apex. Altogether, these results demonstrated that the potential of KPFM to monitor protein interactions goes beyond the protein-molecule level, as in the case of PKs (Figure 4a), and can also be useful in monitoring protein-NP interactions (Figure 4e).

3.2. Direct Detection of Collagen Fibrils Using KPFM

Collagen fibrils, a ubiquitous class of structural and complex proteins, are central to the mechanical and biological integrity of tissues such as tendon, skin, bone, and connective tissue.[85,86] Far from being mere nanoscale "cables," these fibrils exhibit complex physicochemical properties—most notably, surface charge and mechanical responsiveness—that critically influence cell–matrix interactions.[87,88] Among their most intriguing features is piezoelectricity, the generation of electrical charge in response to mechanical stress, which has been probed at the nanometre scale using piezoelectric force microscopy (PFM).[89,90] Such high-resolution studies have uncovered collagen's capacity to function as a dynamic electromechanical interface, with far-reaching implications for tissue homeostasis, cellular adhesion, and the design of next-generation scaffolds in regenerative medicine.[91,92]

In the context of collagen, investigating the ESP can provide key insights into its functional role under physiological and engineered conditions.[27,93] For instance, in a landmark study, KPFM was applied to native type I collagen fibrils extracted from mammalian tendons and mounted on stretchable polymer substrates.[94] (**Figure 5a**). This approach enabled real-time visualization of how ESP evolves under mechanical strain. Remarkably, KPFM revealed that as strain increased up to 10% (Figure 5b), the ESP shifted toward more positive values, indicating a reorganization of surface functional groups, likely involving the exposure of amines. However, at strains beyond 10% and up to 17%, the ESP reversed polarity, becoming increasingly negative (Figure 5c), consistent with the exposure of carboxyl moieties. These findings uncovered a nonlinear electromechanical response in collagen and opened new avenues for understanding its functional role in mechanobiology and biomaterials design.

Beyond its ability to probe mechanical stress–chemical modification relationships, KPFM has also proven powerful in elucidating chemical changes to collagen, particularly within pathological microenvironments. One such study demonstrated that glycation of collagen fibrils by ribose-5-phosphate (R5P)—a process relevant in metabolically active tissues such as tumors—disrupts their longitudinal molecular organization[95] (Figure 5d,e). KPFM analysis showed that R5P-glycated fibrils display a significantly more negative ESP compared to native collagen (Figure 5e), indicating that glycation induces marked changes in the fibril's electrostatic landscape. Similarly, exposure to methylglyoxal (MGO)—a reactive carbonyl compound implicated in aging and diabetes—was found to simultaneously alter mechanical and electrostatic properties.[27] Combining AFM nanoindentation with KPFM, researchers observed three key

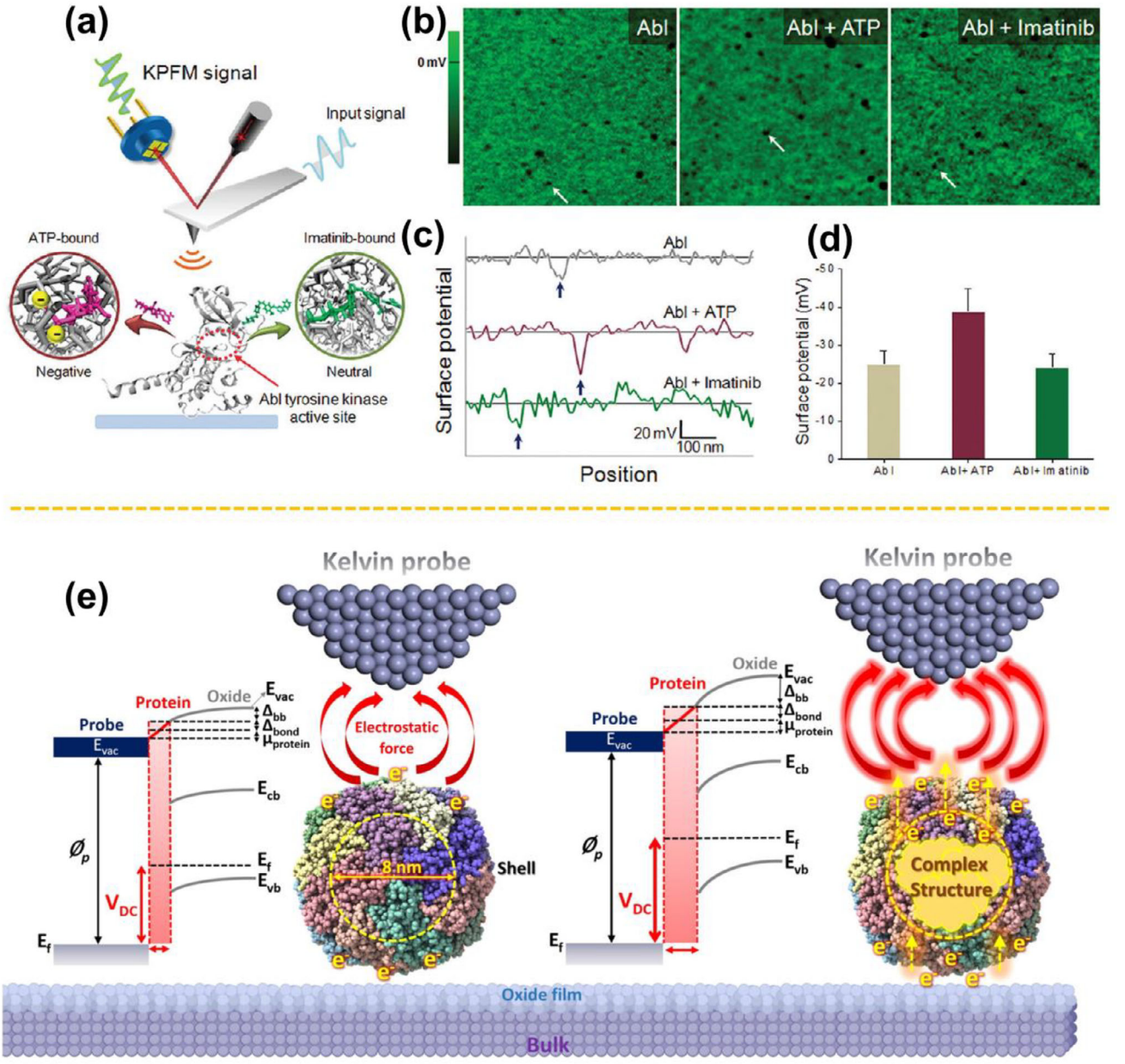

Figure 4. a) Schematic representation for the identification and quantification of Abl Tyrosine kinases bound to ATP, b) KPFM images showing Abl tyrosine kinases (indicated by white arrows) in their unbound state (left), ATP-bound state (middle), and Imatinib-inhibited state (right). c) Corresponding ESP profiles of Abl tyrosine kinase in these three states. d) Average ESP values of Abl tyrosine kinases in the unbound, ATP-bound, and inhibited states. Adapted with permission.[8] Copyright 2011, American Chemical Society. e) Schematic representation of the KPFM principle and corresponding energy level diagram illustrating the electrostatic interaction between a highly conductive AFM tip apex and a single fresh or a filled-apoferritin molecule on the oxide-bulk matrix at the atomic scale. The presence of a complex cluster within the internal cavity of the apoferritin molecule can markedly influence the energy level diagram, modify the ESP, and alter the intensity of the electrostatic forces. Adapted with permission.[20] Copyright 2024, American Chemical Society.

effects: a) a substantial increase in nanostiffness, b) a reduction in ESP, and c) a shift in hydration state. Notably, the absence of a strong correlation between stiffness and ESP suggested that distinct molecular mechanisms govern these changes. Once again, it was KPFM that revealed the nuanced electrostatic alterations accompanying chemical modification at the single-fibril level.

3.3. KPFM Applications in Protein Biosensing, Diagnostics, and Drug Screening on Conductive Surfaces

By enabling direct probing of protein properties with high sensitivity to ESP variations, KPFM has immense potential to bridge fundamental biophysical understanding with applied biomedical innovation and bioelectronic technologies.[96]

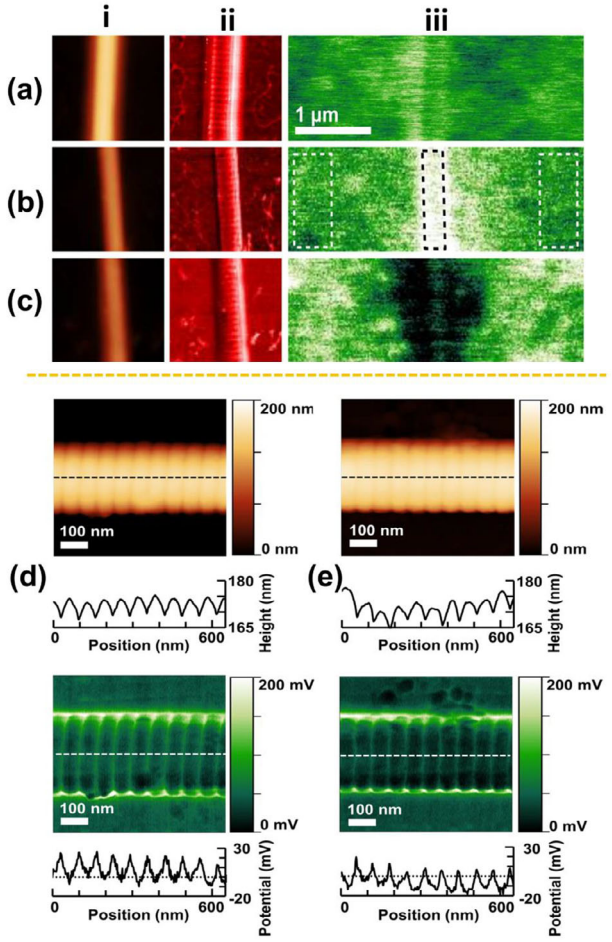

Figure 5. An Illustration of stretching and releasing a native collagen fibril on a polydimethylsiloxane (PDMS) film through three stages: a) unstrained (before stretching), b) strained (after stretching), and c) after releasing from strain. Columns represent: i) tapping-mode height images (200 nm color range), ii) tapping-mode phase images (20° color range), and iii) ESP maps (100 mV color range) corresponding to the same locations as (i) and (ii). The fibrils were not hydrated with buffer or deionized water at any stage of the process. The horizontal scale bar in (a, iii) is consistent across all images. In (b, iii), white rectangles on the sides of the fibril were used to determine the absolute PDMS potential, while the black rectangle at the center indicates the area for absolute fibril potential measurements, positioned using the AFM topography image in (b, i). The relative fibril potential shown in column (iii) was calculated by subtracting the absolute PDMS potential from the absolute fibril potential, with lighter pixels indicating a more positive potential. Adapted with permission.[94] Copyright 2021, American Chemical Society. AFM topography, KPFM ESP maps alongside corresponding longitudinal height and ESP profiles (derived from the dashed lines in each section) representing collagen fibril in d) unglycated and e) R5P-glycated conditions. ESP values are measured relative to the HOPG baseline. Adapted with permission.[95] Copyright 2020, Springer Nature.

Building on its capacity to identify subtle electronic characteristics that govern protein functionality, and recognizing that early diagnostics and drug screening rely on highly sensitive and selective biomolecular detection, this subsection explores KPFM's potential to analyze protein physicochemical interactions on functionalized conductive surfaces, which have laid the groundwork for advancements in bioelectronics.[97]

In recent decades, CNT surfaces have emerged as a focal point in bioanalytical research due to their conductivity, specificity, sensitivity, and capacity for accurate quantitative analysis.[98] Integrating horizontally aligned CNTs with KPFM imaging enables the generation of sensing devices with unprecedented ultrasensitive detection and precise quantification of biomolecular interactions. This combination has proven effective in verifying the specificity of various proteins, such as human serum albumin (HSA), fibrinogen, and transferrin, when drop-casted onto aptamer-functionalized carbon nanotubes (ACNTs) as part of a bioassay.[23] In particular, AFM and KPFM analyses revealed that the surface morphology and ESP of ACNTs remain unchanged upon exposure to HSA, transferrin, and fibrinogen, indicating minimal nonspecific physisorption (**Figure 6**a,b). Strikingly, a significant shift in ESP was observed following exposure to thrombin (Figure 6b), underscoring a distinct and specific interaction between ACNTs and thrombin compared to the other proteins.[23]

Crucially, the high sensitivity of these KPFM-based bionanosensors extends beyond simple protein assays, holding potential for other diagnostic challenges, such as the early detection of cancer. Here, the ability to identify rare, low-concentration biomarkers such as carcinoembryonic antigens (CEAs) becomes particularly important. However, the low expression of these markers complicates the task, making the development of reliable detection methods even more pressing.

Considering such limitations, a biosensor platform integrated with KPFM has been developed for detecting CEAs on circulating tumor cells (CTCs).[98] In this research, AFM and KPFM measurements were conducted on a CNT-based sensor before and after antigen treatment. Bare and antigen-modified ACNTs were characterized by a similar height of 4.0 ± 0.3 nm. However, while the Φ of bare ACNTS was 21.7 ± 4.6 mV, a pronounced decrease in ESP was observed following antigen binding, resulting in a value of $\Phi = -93.9 \pm 13.7$ mV. To quantitatively analyze the binding of CEACAM5 (the carcinoembryonic antigen-related cell-adhesion molecule 5) proteins to ACNT, a lysate solution of cancer cells was introduced to the ACNT surface. The binding of CEACAM5 proteins was evidenced by an increase in ACNT height ($h \approx 6.4$ nm) and ESP ($\Phi \approx 80$ mV). As previously outlined, the synergy between KPFM and ACNTs represents a robust and versatile platform for the precise quantification of biomolecules relevant to disease pathology.

Metallic conductive surfaces, particularly gold (Au), have also been extensively studied in combination with KPFM to monitor the dielectric properties of biolayers, driven by protein dipoles and polarization density. These properties are crucial for bioelectronics, where reproducibility is paramount. Traditionally, the incorporation of antibodies on Au relies on superficial physisorption, in contrast to the covalent binding observed with CNTs. While covalent attachment is often favored for its stability, physisorption presents notable advantages, including scalable fabrication without compromising stability. This balance is especially relevant for developing bioelectronic platforms.

In this context, the ESP of anti-Immunoglobulin M (anti-IgM)—a common antibody[99]— was investigated using KPFM. The focus was on antibody biolayers physisorbed onto Au

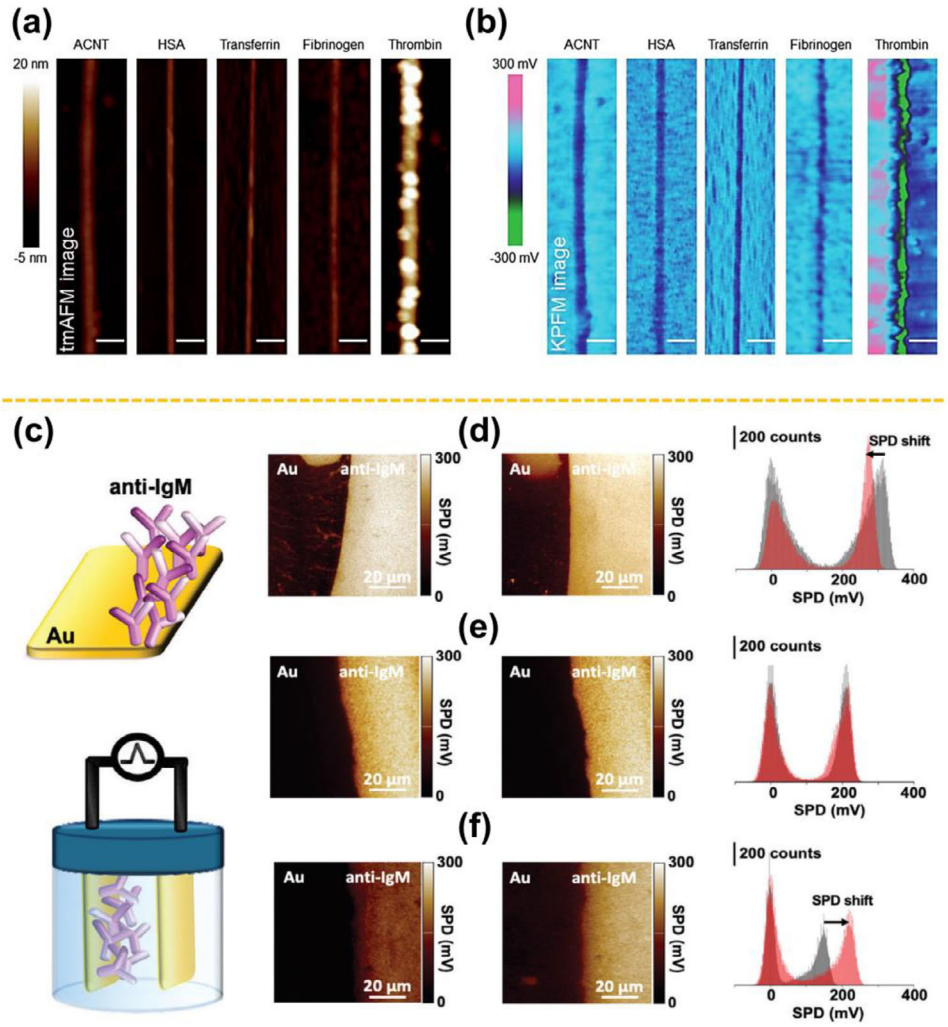

Figure 6. a) tmAFM images and b) KPFM images of ACNTs treated with solutions of human serum albumin (HSA), transferrin, fibrinogen, and thrombin. Adapted with permission[23] Copyright 2012, The Royal Society of Chemistry. c) Illustration of an anti-IgM layer adsorbed onto an Au substrate, showing a well-defined Au/anti-IgM interface alongside a schematic of the experimental setup, wherein a cell containing deionized water undergoes electric field cycling by applying a potential sweep between an anti-IgM-modified electrode and a gold counter electrode over the range [0.1, −0.5 V] for 20 cycles. d) KPFM image of the anti-IgM layer before EF-cycling, at the interface with the bare Au substrate (left), and post EF-cycling for the same region (right). ESP histogram analysis comparing pristine (black) and post-cycling (red) samples, showing a noticeable shift toward higher ESP values. e) Analogous measurements for a second sample, confirming that EF-cycling does not alter the ESP distribution proven from the corresponding histogram analysis. f) ESP analysis for a third sample, indicating a shift toward lower values following EF-cycling. Adapted with permission.[96] Copyright 2024, Wiley-VCH GmbH.

substrates, examined both before and after exposure to electric field (EF) cycling[96] (Figure 6c). KPFM mapping of the Au/anti-IgM regions revealed an average ESP of 306 ± 27 mV, establishing a baseline signal (Figure 6d) that showed a reduction in both the ESP energy ($\Phi_{S,biolayer}$) and work function ($\Phi_{biolayer}$) compared to bare Au, caused by the anti-IgM deposition. After EF cycling, the same region was re-imaged, showing a reduced ESP of 252 ± 9 mV (histogram analysis in Figure 6d). This decrease confirmed the sensitivity of KPFM in detecting protein depolarization induced by the EF cycling. However, KPFM images of a second sample (Figure 6e), where the ESP remains constant, are shown. Meanwhile, Figure 6f presents a third sample where the ESP increases. It is important to clarify that while the $\Phi_{S,biolayer/e}$ values upon EF cycling can either decrease or increase relative to Au, depending on the sample, the $\Phi_{S,biolayer/e}$ always decreases (compared to Au) when the biolayer is deposited on the gold substrate.

Overall, the application of KPFM to protein systems has evolved beyond structural characterization to probing functional electrostatics, notably the ESP at the single-molecule level. Across diverse examples—including kinase–ligand binding, apoferritin–nanoparticle interactions, and collagen's mechanoelectrical response—KPFM has revealed subtle physicochemical changes in ESP that underpin biological function and dysfunction. However, these advances remain largely confined to proof-of-concept studies. From a practical perspective, the quantitative interpretation of KPFM data—crucial for sensing and diagnostics—is still hindered by biological variability, substrate effects, probe artefacts, and

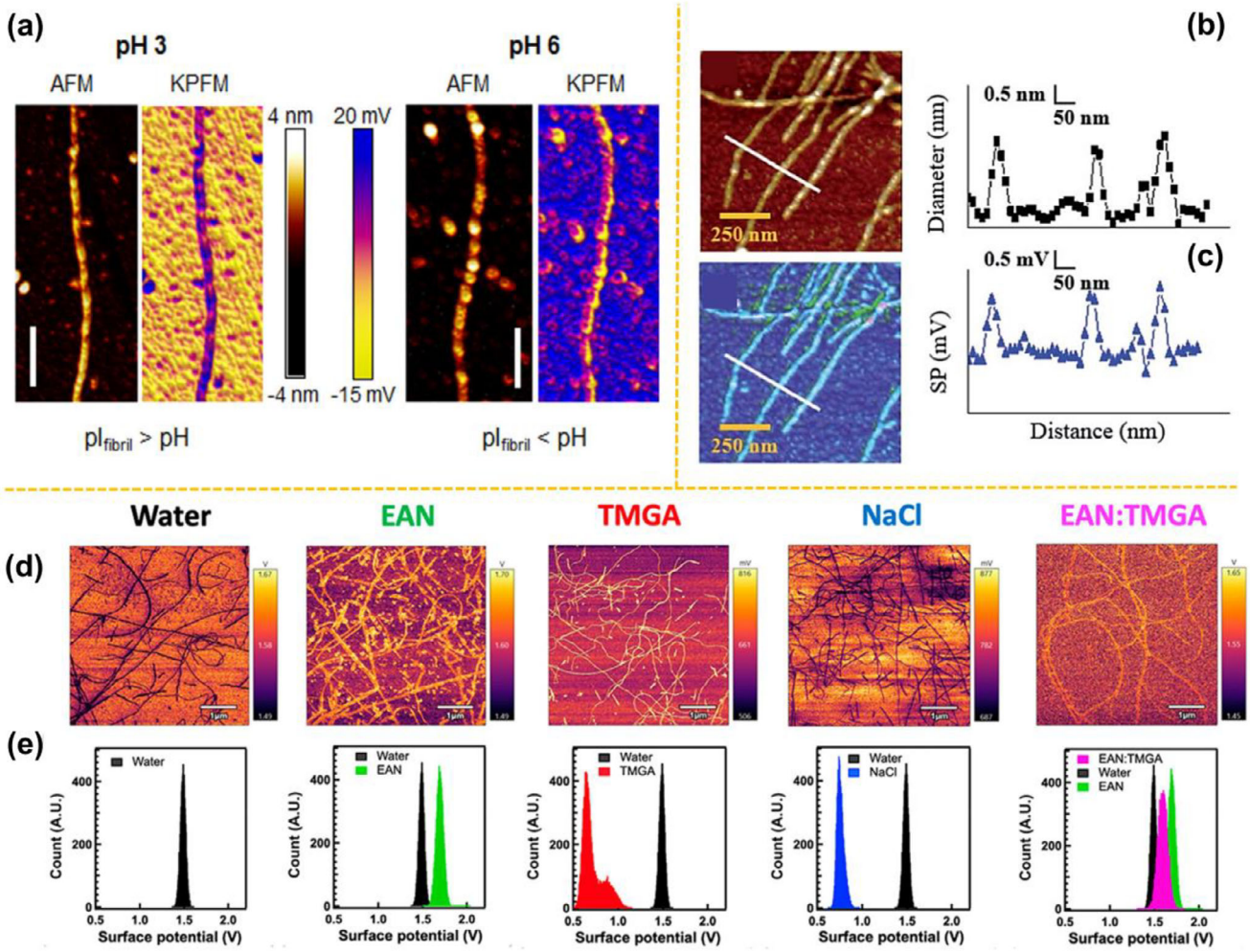

Figure 7. a) AFM topology and ESP images of β-lactoglobulin amyloid fibrils prepared in buffer solutions at pH 3 and 6, with each image featuring a 250 nm scale bar. Adapted with permission.[28] Copyright 2012, American Institute of Physics. KPFM map of the electrical properties of regrown amyloid fibrils that originated from fragmented fibrils. b) Topological and c) ESP images alongside corresponding cross-sectional topological and ESP profiles (obtained from line scans, white lines) of the original amyloid fibrils. Adapted with permission.[104] Copyright 2014, The Royal Society of Chemistry. Representative surface electric potential OL-EPM images d) along with their associated histogram distributions e) for lysozyme amyloid fibrils incubated in sole water (black), water solutions of EAN (green), TMGA (red), and NaCl (blue) at a molar ratio of 3.5 ILs per protein, and in water solutions of EAN: TMGA at 1:3.5 molar ratio. The distributions in panel e) are not limited to the data in panel (d) but have been obtained using all the sets of OL-EPM data. Adapted with permission.[106] Copyright 2022, American Chemical Society.

signal delocalization, all of which complicate cross-system generalization.

To advance beyond proof-of-concept and enable real impact in protein biosensing and diagnostics, the field must prioritize the standardization of measurement protocols, the development of more robust quantitative models for ESP interpretation, and the integration of KPFM with fluidics, environmental control, and automation. With such developments, KPFM could evolve from a specialized surface probe into a functional sensing platform for diagnostics, protein engineering, and drug screening.

4. Direct Detection of Amyloid Fibrils Using KPFM

The utility of KPFM in mapping nanoscale electrostatics extends beyond collagen to amyloid fibrils, whose aggregation underlies the pathogenesis of neurodegenerative diseases such as Alzheimer's and Parkinson's.[100–102] Amyloidogenesis is governed in part by electrostatic interactions with surrounding biomolecules, such as nucleic acids and glycosaminoglycans, that facilitate fibril aggregation and contribute to cytotoxicity via membrane disruption.[103] To visualize these interactions, KPFM was employed to map the ESP of β-lactoglobulin amyloid fibrils on Si under varying pH conditions.[28] The results revealed that surface charge distribution is highly dependent on fibril conformation and solvent environment, enabling the estimation of the fibril's isoelectric point (pI) (**Figure** 7a). These findings provided critical insight into the electrostatic basis of amyloid-driven cellular dysfunction, reinforcing KPFM as a powerful technique for probing the physicochemical forces that govern protein misfolding and aggregation.

These results prompted further studies into the structural and electrical characteristics of both original and regrown

β-lactoglobulin (β-lg) fibrils.[104] In this research, KPFM analysis was carried out on a silicon substrate to directly compare these properties before and after regrowth. The topographical (Figure 7b) and ESP (Figure 7c) images alongside the corresponding height and ESP line profiles of the original β-lg fibrils (prior to ultrasonication) revealed an average diameter of 1.76 ± 0.54 nm and a measured ESP of 11.38 ± 6.87 mV, consistent with earlier reports.[28] After fibril regrowth (after sonication), the average fibril size was 2.65 ± 0.66 nm in diameter and had an ESP of 16.76 ± 6.6 mV. The similarity between the before and after regrowth enabled to conclude that β-lg fibrils can be regrown without losing their original characteristics.

Amyloid fibrils are also well known for their diverse morphologies and assembly pathways, which in turn give rise to distinct mechanical properties and surface charge distributions. These features critically influence how amyloid fibrils engage with other biomolecules and cells, underscoring the importance of the ESP in these interactions.[105] In this context, a prior study employed OL-EPM to map the ESP of amyloid fibrils formed under various conditions.[106] The results revealed distinct mean ESP: 1.67 ± 0.01 V in ethylammonium nitrate (EAN) solution, 0.67 ± 0.1 V in tetramethyl-guanidinium acetate (TMGA) solution, 0.73 ± 0.05 V in NaCl solution, 1.57 ± 0.01 V in an EAN: TMGA 1:3.5 mixture, and 1.48 ± 0.01 V in pure water (Figure 7d,e). These values exhibited a strong correlation with the average heights of the fibrils, offering compelling evidence for the presence of two distinct amyloidogenic pathways in EAN and TMGA solutions. Such differences in the amyloidogenic pathways not only shape the morphological features of the fibrils but also suggest ESP variations in their interactions with biological environments and systems.[106] These findings highlight how the physicochemical properties of amyloid fibrils can be modulated by their environment, with important implications for their biological activity and potential impact on cellular systems.

While these foundational studies established the application of KPFM in amyloid research, significant challenges remain in translating the nanoscale ESP landscapes of amyloid fibrils into biologically relevant contexts. To fully realize the potential of KPFM in amyloid research, future efforts should prioritize real-time imaging of amyloid dynamics within physiologically representative systems, such as lipid bilayers or cell-mimicking environments,[107,108] ideally integrated with complementary readouts such as redox activity or mechanical compliance. Bridging these experimental advances with mechanistic insights could substantially improve our understanding of amyloid pathology and guide the development of therapeutic strategies against protein misfolding disorders.[109]

5. KPFM Insights into Lipid-Based Biomimetic and Gene Delivery Platforms

Lipids are fundamental amphiphilic molecules composed of hydrophilic head groups and hydrophobic tails, whose self-assembly into bilayers underpins the architecture of cellular membranes. These bilayers—primarily composed of phospholipids, cholesterol, and glycolipids—create dynamic, semi-permeable barriers that regulate molecular transport, facilitate signal transduction, and preserve cellular homeostasis. Their ability to form ordered yet flexible structures makes them essential not only for cellular function but also for the design of biomimetic systems such as gene delivery platforms.

In this context, gemini surfactants (GSs) have emerged as promising vectors for DNA delivery due to their strong electrostatic interactions with negatively charged DNA and their tunable molecular architecture.[110–112] Unlike conventional surfactants, GSs consist of two hydrophobic tails linked by a spacer, allowing their physicochemical properties to be finely adjusted by modifying tail length, spacer flexibility, or by introducing functional groups.[113] Their positively charged head groups promote DNA binding and condensation, thereby improving their effectiveness as gene carriers.[114,115]

To understand these interactions and optimize DNA loading and delivery, researchers initially computationally modelled GS monolayers mixed with lipids such as 1,2-dioleoyl-sn-glycero-3-phosphocholine (DOPC) as simplified systems.[116,117] These theoretical studies illuminated the electrostatic and hydrophobic forces governing complex formation and revealed that lipid incorporation significantly enhances transfection efficiency.[118,119] To experimentally probe these effects, various characterization techniques have been used, including fluorescence microscopy,[120] Brewster angle microscopy (BAM),[121] AFM, and KPFM.[122,123] Notably, AFM revealed morphological changes in GS–lipid monolayers upon DNA binding,[124,125] while KPFM was instrumental in enabling precise mapping of ESP distributions, highlighting how DNA alters electrostatic profiles of the GS-lipid system.[126,127]

Building upon these insights, researchers developed lipid–GS monolayers incorporating lipids commonly found in biological membranes and used them as advanced model systems to better mimic cellular interfaces and monitor DNA binding during monolayer formation.[126] KPFM-based topographical and electrostatic characterization of these monolayers, both with and without DNA, revealed striking differences, uncovering regions of significantly elevated ESP, particularly in domains situated between lipids with and without adsorbed DNA strands, which remained undetectable by conventional imaging techniques (**Figure 8a**). As we have seen above, among the characterization techniques available to characterize GS-lipid systems, only KPFM provides the resolution and sensitivity required to detect these localized electrostatic anomalies, offering unprecedented insight into how DNA integration modifies GS–lipid interfaces.

Extending the use of KPFM to probe the role of surfactant architecture, a subsequent study investigated gene delivery systems composed of DOPC, 1,2-dipalmitoyl-sn-glycero-3-phosphocholine (DPPC), and GSs of the type *N,N*-bis(dimethylalkyl)-α,ω-alkanediammonium dibromide in varying ratios.[128] By combining AFM and KPFM, researchers examined how alkyl chain length in GSs influences both structural organization and electrostatic properties of the monolayers.[128] In pure DOPC–DPPC systems without GS, stable nanoscale domains were observed, with only minor changes in domain height and ESP upon addition of GS-12 (12-carbon chain). In contrast, GS-16 (16-carbon chain) led to tighter lipid packing, more complex domain architectures, and a significant ESP increase—from 336 to 658 mV (ΔV = 322 mV). These findings reinforced the importance of molecular design, demonstrating

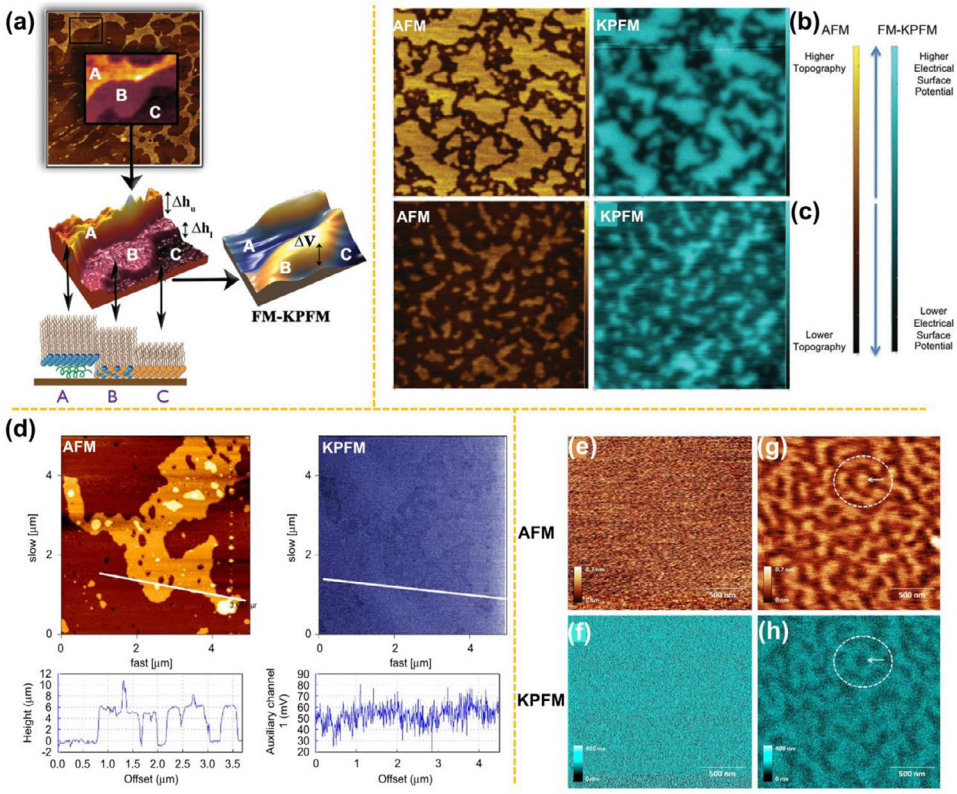

Figure 8. a) Displayed here is a 3D rendering derived from the AFM topography, identifying three regions (A, B, and C) with height differences (Δh_l and Δh_u) as illustrated schematically at the bottom of the 3D image. To the right, the FM-KPFM signal's 3D rendering for the same region visualizes the electrical potential difference (ΔV) associated with the mid-height region (B). The schematic below highlights DNA (green) attached to a monolayer of lipids (gold) and gemini surfactant (blue). Adapted with permission.[126] Copyright 2021, The Royal Society of Chemistry. AFM (gold) and FM-KPFM (blue) imaging highlight the impact of cholesterol on the topography and ESP of a dipalmitoylphosphatidylcholine - 1,2-dioleoyl-sn-glycero-3 phosphocholine DPPC–DOPC lipid mixture. b) Display AFM and FM-KPFM scans of DPPC–DOPC mixture (607:393 ratio), respectively. In comparison, c) images show corresponding scans for a DPPC–DOPC–cholesterol sample (560:346:94 ratio). All measurements were performed under ambient air conditions, with 2 × 2 µm scan areas. Bright regions represent higher topography or ESP, while darker regions reflect lower values, as indicated by the scale bars on the right. Adapted with permission.[132] Copyright 2017, The Royal Society of Chemistry. d) topography and KPFM images alongside corresponding line profiles of a DPPC/eggPG lipid film without SP-C, and a DPPC/eggPG/SP-C film. The lipid films were deposited onto mica using the Langmuir–Blodgett technique at a compression of 48 mN m^{-1} and imaged in air. Adapted with permission.[122] Copyright 2009, Elsevier. AFM and corresponding FM-KPFM images of lipid monolayers e,f) without and g,h) with cholesterol: AFM topography images of (e) a pure DOPC monolayer and (g) a DOPC monolayer containing 20% cholesterol; corresponding FM-KPFM images showing the ESP distribution of the pure DOPC monolayer and the DOPC monolayer with 20% cholesterol. AFM and FM-KPFM imaging were performed using a SmartSPM (AIST-NT) system. The arrow within the circular region indicates that areas enriched with cholesterol are elevated in topography but exhibit lower ESP. Adapted with permission.[133] Copyright 2012, Cell Press.

that longer GS chains enhance domain stability and amplify ESP, thus underscoring the central role of KPFM in linking structural modifications to functional electrostatic behavior in lipid-based gene delivery platforms.

Until now, only simplified lipid systems have been discussed. However, in biologically relevant contexts, the molecular arrangement of lipids in biomembranes gives rise to intricate film morphologies with regions of distinct ESP.[129–131] This electrostatic heterogeneity has been effectively captured using KPFM, which, for instance, revealed how cholesterol modulates both the topography and ESP of DPPC–DOPC monolayers.[132] In the absence of cholesterol, distinct domains were visible with a height difference (Δh) of 1.22 ± 0.03 nm, attributed to ordered DPPC-rich regions compared to disordered DOPC areas. These domains also exhibited a mean ESP difference (ΔV) of 41.6 ± 5.39 mV (Figure 8b). Upon cholesterol addition, smaller domains formed with a reduced Δh of 0.97 ± 0.06 nm, consistent with cholesterol-induced disorder, and the ΔV increased to 67.25 ± 7.03 mV (Figure 8c).

In line with these findings, other studies have employed KPFM to investigate more complex and biologically relevant systems. For example, KPFM was used to examine how surface compression and the pulmonary surfactant protein C (SP-C) affect the structure and ESP distribution of lipid monolayers.[122] A model of an artificial lung surfactant—composed of DPPC, egg phosphatidylglycerol (eggPG), and SP-C—was analyzed. Notably, the introduction of SP-C led to an enhanced ESP signal contrast within the DPPC/eggPG monolayer. In contrast, lipid patches lacking SP-C exhibited minimal contrast in ESP, measuring only a few millivolts (Figure 8d). In a separate study investigating the interplay between membrane composition and amyloid beta (Aβ) peptide interaction, researchers examined how cholesterol

affects fibril formation and cytotoxicity.[133] ESP measurements revealed that pure lipid monolayers exhibited smooth, featureless ESP maps (Figure 8e,f), while the addition of 20% cholesterol introduced an ESP difference of 61 ± 8 mV (Figure 8g,h). These results suggest that cholesterol may act as a molecular anchor, enhancing the binding affinity of amyloidogenic peptides to membrane surfaces. Altogether, these findings demonstrate that KPFM's ability to detect ESP extends beyond idealized conditions and can be effectively applied to biologically relevant, real-world systems.

Despite recent studies that have begun to explore lipid-based systems in biologically relevant environments—where hydration, lipid diversity, and dynamic molecular interactions play critical roles—further efforts are needed to apply KPFM to supported bilayers or vesicles under near-physiological conditions. Integrating complementary techniques, such as fluorescence microscopy[134] or functionalized sensitive probes,[135] alongside continued advances in liquid-compatible KPFM modalities, will be essential to fully realize its potential in membrane biophysics and bioengineering.

6. KPFM in DNA-Based Research

6.1. Optimizing KPFM Conditions for High-Resolution Mapping of DNA ESP

Electrostatic interactions are fundamental forces governing the behavior of oligonucleotides—short strands of DNA or RNA—particularly in their interactions with other biomolecules and ions.[33,136] These interactions are largely governed by the ESPs of the interacting species, which, in turn, influence critical structural and functional properties of oligonucleotides, including their hydrophobicity, hybridization behavior, and overall conformational stability.[137] Despite their central role, accurately quantifying the ESP of individual biomolecules such as DNA, especially at the nanoscale, remains a major experimental challenge. To begin addressing this gap, several works have proposed modifications in the KPFM's setup to directly probe the electrostatic landscape of DNA with nanometre precision, offering new opportunities to investigate ESP distributions at the single-molecule level.

In one such study, researchers modified conventional Si-based AFM tips with AuNPs. This modification enabled precise detection of approximately 2700 base-pair double-stranded plasmid DNA adsorbed onto freshly cleaved mica surfaces, offering deeper insights into molecular-level electrostatic interactions.[138] The experiment employed FM topography and force gradient KPFM, minimizing applied forces and preventing direct contact with biomolecules—ideal for imaging delicate samples like DNA.[139] The resulting topographic image (**Figure 9a**) displayed a DNA structure approximately 0.5 nm in height and 11 nm in width (FWHM),[140] as shown in the cross-sectional profile in Figure 9c. Moreover, KPFM measurements of the double-stranded plasmid DNA on mica showed that ESP variations impacted the signal-to-noise ratio. By applying a 5 V bias voltage, researchers improved contrast and determined that the DNA ESP ranged from −100 to −150 mV relative to the mica substrate Figure 9b.

In addition to tip composition, substrate properties can also critically affect the measured ESP of DNA. For instance, it was found that silicon-based substrates with native oxide layers offer a distinct electrostatic environment to mica that can enable more stable and reproducible measurements, particularly when probing DNA–substrate interactions at the nanoscale.[44] A study investigating a 3000-base-pair circular double-stranded plasmid DNA on such silicon substrates found that this setup not only yielded more consistent measurements but also allowed clearer exploration of DNA–substrate electrostatics.

To gain further insights into these interactions, the effect of measurement mode was also tested using AM and DFM.[44] In AM mode, at an average tip–sample separation of 47 nm, no electrostatic signal was detected from the DNA (Figure 9d,e). However, reducing the tip–DNA separation to 32 nm (Figure 9f) and then 24 nm (Figure 9g) led to a gradual increase in the measured negative ESP, which reached ≈−7 mV relative to the silicon background. Conversely, DFM-KPFM imaging using the same tip revealed a much more negative ESP, averaging around −120 mV (Figure 9h,i). These findings demonstrate that even under identical conditions and minimized working distances, the sensitivity of AM-KPFM in characterizing DNA ESP remained at least an order of magnitude lower than that of DFM-KPFM.

Despite its lower sensitivity compared to DFM, AM-KPFM remains highly valuable for studying soft biological materials, where minimal perturbation, ambient compatibility, and straightforward implementation are essential. These characteristics make it particularly well-suited for investigating DNA–metal ion interactions, where maintaining molecular integrity is crucial. This is especially relevant given the strong affinities of nucleic acids and nucleobases for specific toxic metal ions, positioning DNA as a promising scaffold for metal ion sensing applications.[142–150] In this context, recent work demonstrated that AM-KPFM can achieve ultra-sensitive detection of silver ions using Ag^+-specific DNA confined to a single droplet. By mapping ESP differences, the technique clearly distinguished Ag^+-bound DNA from its unbound counterpart, revealing a ≈40 mV increase upon Ag^+ coordination and charge neutralization (Figure 9j).[141] These findings underscore the precision and practical utility of KPFM—even in AM mode—for resolving subtle ion-binding events in biologically relevant environments.

6.2. KPFM Applications for Diagnostics and Biosensing on DNA-Functionalized Nanosurfaces

Current optical methods for genetic detection using DNA-capped AuNPs (DCNPs)—including scanometric assays,[151] colorimetric techniques,[152,153] and surface-enhanced Raman spectroscopy (SERS)[154,155]—are limited by several persistent challenges. These include the need for large sample volumes, inconsistencies arising from uneven DCNP distribution, and interference from residual chemicals, all of which can undermine detection accuracy.[156] Furthermore, non-specific binding events reduce specificity, complicating the detection of weak or transient biomolecular interactions.[157,158] To overcome these limitations, recent efforts have integrated KPFM with DCNP-based detection, providing an innovative route to enhance sensitivity and specificity. By confining the interaction domain, this combined

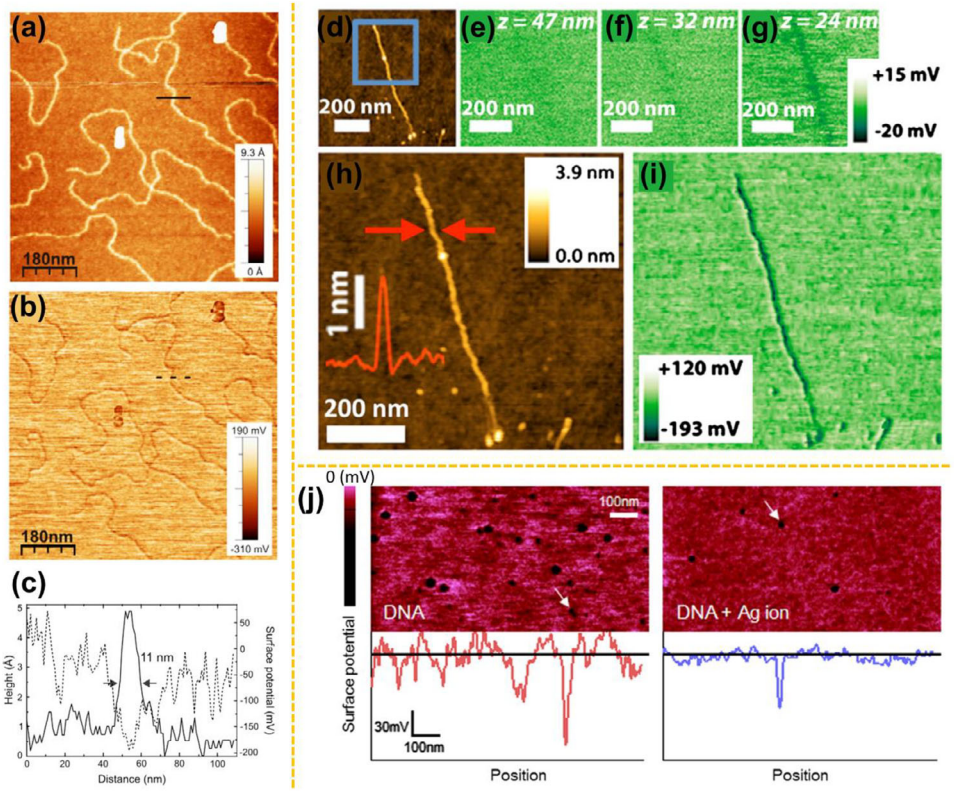

Figure 9. AFM and KPFM imaging of DNA deposited on mica was acquired using a gold nanoparticle (Au NP)-coated tip. a) Topographic and b) ESP images of dsDNA molecules were simultaneously obtained in FM-topography mode. c) Cross-section profiles along the indicated lines in the topographic (solid line) and ESP (dashed line) images are shown, acquired in single-pass mode. Adapted with permission.[138] copyright 2013, Institute of Physics (IOP). d) Topographical and ESP scans were acquired over a cluster of aligned DNA duplexes at average tip-sample distances of e) 47 nm, f) 32 nm, and g) 24 nm using AM-KPFM in lift mode. The potential scans correspond to the boxed region in (d). h,i) Topographic and ESP maps of the same DNA structure imaged using DFM-KPFM. Adapted with permission.[44] copyright 2010, American Institute of Physics (AIP). j) KPFM images and corresponding line profiles show double-strand DNA (indicated by white arrows) in its unbound state and its bound state with silver ions. Adapted with permission.[141] Copyright 2014, Elsevier.

approach significantly reduces non-specific binding and enables the detection of subtle ESP variations with high spatial resolution. This is especially critical for real-time molecular diagnostics and precision bioassays.[156]

In this context, high-loading DCNPs (≈2000 DNA molecules per ≈100 nm AuNP) were shown to establish a robust statistical foundation for bioassay analysis, enabling the reliable detection of specific nucleic acid sequences, even when only subtle ESP shifts occur, such as those caused by single-point mutations.[156] However, the study also highlighted a critical parameter affecting detection accuracy: the underlying substrate. Measured ESP values of DCNPs differed significantly across substrates, ranging from -1.45 ± 0.06 V on Au to -1.51 ± 0.21 V on p-type Si, -1.25 ± 0.16 V on SiO_2, and -1.30 ± 0.20 V on Fe (**Figure 10**a–c), indicating that substrate-induced potential variations can strongly influence assay performance.

For precise point mutation detection, an experiment was conducted to assess the interaction between probe-DNA-modified DCNPs (p-DCNPs) and non-complementary target DNA (*t*DNA), as ncDNA. The KPFM result of p-ncDCNPs ($\phi \approx 0.747$ V) closely matched the ESP of unexposed p-DCNPs ($\phi \approx 0.743$ V), indicating minimal interaction with ncDNA (Figure 10d).[159] Beyond sequence detection, the precision of KPFM-DCNP integration also enables single-nucleotide resolution, a key advancement for improving disease phenotype predictions[160] and developing next-generation diagnostic tools.[161] For example, a KPFM-based DNA bioassay was used to detect 1–5 mismatches (χ_0 to χ_5) in the BRCA1 gene (Figure 10e), revealing a consistent reduction in ESP of p-DCNPs as the number of mismatches increased. This reduction was attributed to fewer hybridization events between probe DNA and *t*DNA, offering a clear, quantifiable signal for mutation detection.[159]

This high sensitivity can also be repurposed for quantitatively monitoring heavy metal exposure, a growing public health concern linked to conditions such as argyria, organ damage, and inflammation, and in extreme cases, fatality.[162,163] In these assays, changes in the ESP of individual p-DCNPs (Figure 10f) are monitored as they interact with *t*DNA in the presence of specific metal ions. For instance, increasing concentrations of Ag^+ (1 pM (Figure 10g) to 10 nM (Figure 10h)) were found to promote cytosine–Ag^+–cytosine base pairing, strengthening coordination bonding, and enhancing the p-DCNPs' ESP. This shift was visualized in the ESP mappings by a progressive color change from black to purple, with signal intensity correlating to Ag^+ concentration, highlighting KPFM's potential for ultrasensitive metal ion detection.

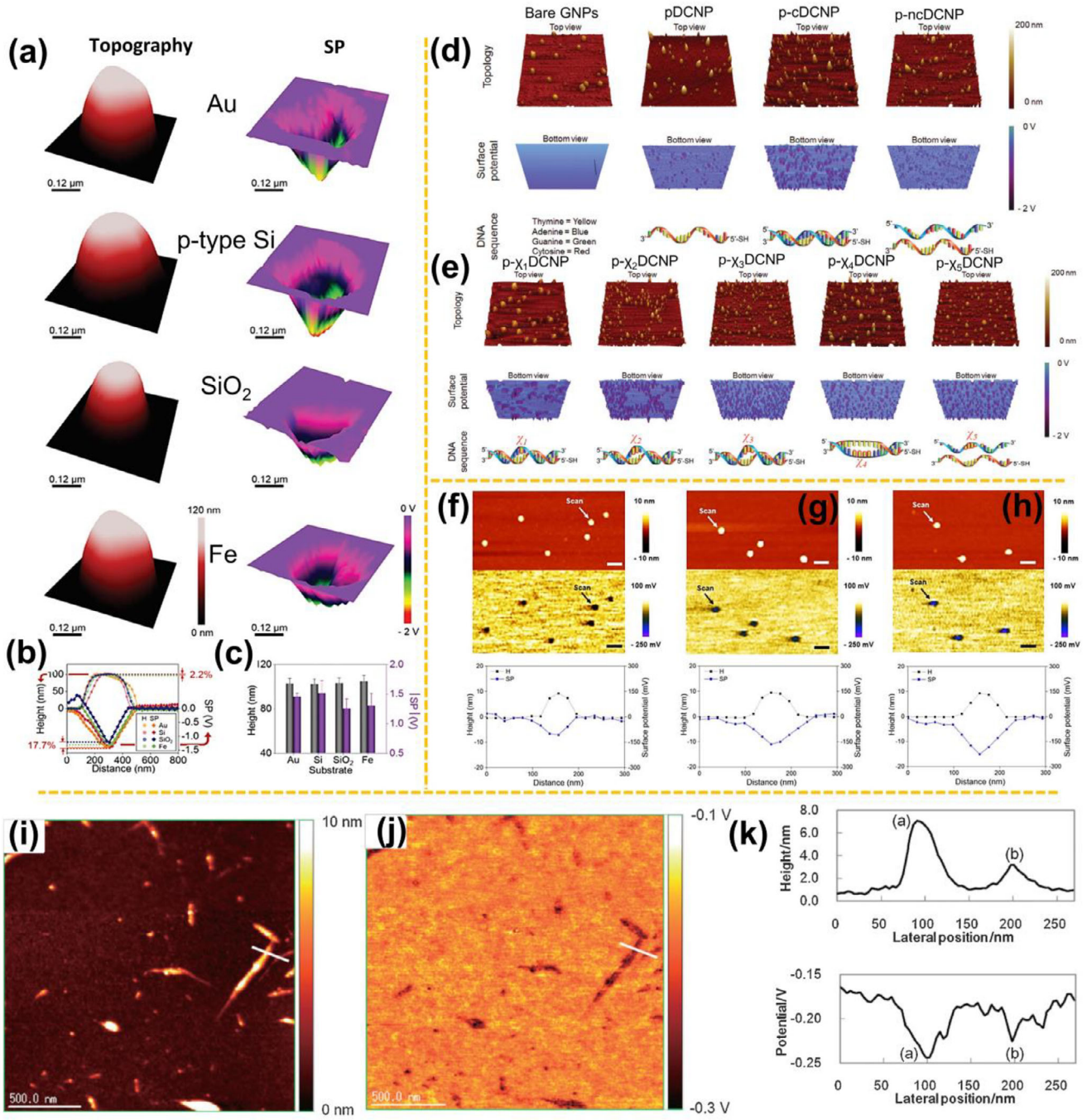

Figure 10. a) 3D topography and ESP images of the DNA-capped gold nanoparticles (DCNP) on four different substrates: Au substrate, p-type Si substrate, SiO_2 substrate, and Fe substrate. Image dimensions are 0.5 × 0.5 μm^2.b) Cross-sectional views of height and ESP measurements across the four substrates. c) Comparative analysis of the average height and SP values of the DCNP on these substrates. Adapted with permission.[156] Copyright 2016, The Royal Society of Chemistry. Bioassay for gene mutation detection using KPFM. d,e) 3D images (10 × 10 μm^2) of DNA-conjugated nanoparticles (DCNPs): top views show topography, and bottom views show ESP. Samples include: (d) bare GNPs (100 nm), pDCNP, p-cDCNP, p-ncDCNP, and (e) p-χ_1DCNP to p-χ_5DCNP. DNA schematics depict hybridization between probe DNA (pDNA) and target DNA (tDNA: complementary, non-complementary, or mutated $\chi_{1-}\chi_5$). Each KPFM image captures the ESP of multiple DCNPs in a single scan. Adapted with permission.[159] Copyright 2018, The Royal Society of Chemistry. AFM height images (top) and KPFM ESP images (bottom) alongside corresponding height and ESP line profiles for DCNPs, including f) DCNPs without Ag+ (negative control), g) DCNPs exposed to 1 pM Ag^+, h) DCNPs exposed to 10 nM Ag^+. White or black arrows in each image indicate the scanned DCNPs corresponding to their respective cross-sectional profiles. The black line depicts the height profile across a single DCNP, The blue line shows the ESP profile aligned with the topographic cross-section. Adapted with permission.[25] Copyright 2018, Institute of Physics (IOP). i) Topography and j) surface-potential images k) alongside corresponding height and ESP line profiles of ss DNA-single walled carbon nanotube (DNA-SWNT) hybrids acquired using KPFM. Scan area: 2 × 2 μm^2; DC bias voltage: −0.12 V; AC modulation frequency: 0.8 kHz; AC modulation voltage: 1.2 V. Adapted with permission.[102] Copyright 2013, Oxford University Press.

Similar to the case of proteins, researchers have begun exploring carbon-based single-walled carbon nanotubes (SWNTs) as alternative nanomaterials to AuNP-based systems for KPFM studies on DNA-based assays and nanobiodevice development[164–167]—a combination that shows strong potential for monitoring molecular interactions and processes. Research in this area has focused on elucidating how DNA molecules interact with SWNT surfaces, thereby modulating their physicochemical behavior and functional performance.

A notable study applied KPFM to characterize SWNTs functionalized with either biological or synthetic molecules.[102] The first stage involved analyzing DNA–SWNT hybrids to assess how DNA adsorption alters SWNTs' ESP. Subsequently, SWNTs modified with polyethylene glycol (PEG) were studied to determine how polymer coatings influence their electronic and surface properties. While single-stranded DNA–SWNTs (ssDNA–SWNTs) exhibited a negative ESP (Figure 10i–k), PEG–SWNTs showed a positive potential, both measured relative to an Au–Pd-coated mica substrate. These results suggest that KPFM could be a powerful tool to distinguish SWNTs modified with different biomolecules.

As demonstrated by the preceding examples, DNA provides a well-defined and highly tunable model for nanoscale electrostatic analysis with KPFM. Although electrostatic interactions have long been recognized as central to oligonucleotide behavior,[168] the direct mapping of their ESP has only recently been enabled by KPFM. This has positioned the technique as a potentially valuable tool for spatially resolving ESP under controlled, biologically relevant conditions—particularly when DNA substrates, tip modifications, and biasing parameters are carefully optimized.

Yet, current application of KPFM remains largely limited to controlled or dry environments, constraining its translational potential in real-world sensing. To overcome these limitations, future efforts should focus on developing liquid-compatible KPFM approaches and establishing standardized probe-functionalization protocols to enable scalable and reproducible DNA-based assays. Additionally, combining KPFM with platforms such as SWNTs or other nanomaterials presents a promising strategy for constructing advanced DNA-based biosensors capable of label-free, ultra-sensitive detection of genetic mutations or environmental toxins.

7. Direct Detection of Cells and Cancer Cells' ESP for Cellular Diagnostics and Targeted Therapies

The plasma membrane serves as a critical interface between the cell and its external environment, maintaining structural integrity while mediating essential physiological interactions.[169,170] Composed of a lipid bilayer, this dynamic architecture supports ionic homeostasis and signal transduction through specialized ion channels, transporters, and glycosylated proteins.[171–173] A key feature of the membrane is the asymmetric distribution of phospholipids, such as phosphatidylserine (PS) and phosphatidylcholine (PC), which is essential for various cellular processes. Disruption of this asymmetry, particularly the externalization of PS, is a well-established marker of apoptosis and other pathological states.[174] Additionally, membrane-associated proteins often carry negatively charged polysaccharide chains, such as sialic acid residues, which modulate the electrochemical profile of the membrane.[175,176] Changes in surface glycosylation and membrane charge are strongly associated with crucial biological events, including apoptosis, differentiation, and oncogenic transformation.[177,178] As such, surface charge distribution serves as a sensitive indicator of cellular state and function.[29]

KPFM offers distinct advantages for assessing the electrostatic properties of cell membranes, as it is relatively insensitive to topographical artifacts and capable of resolving ESP with nanometer-scale resolution.[22,29,30] This makes KPFM especially valuable for exploring molecular-level changes in both normal and cancerous cells, where alterations in ESP often reflect deeper shifts in biochemical activity.[13,179] By leveraging this capability, KPFM has the potential to detect the unique electrostatic signatures associated with malignancy, thereby informing diagnostic strategies and advancing the development of targeted therapies.[3]

These strengths are exemplified in recent studies that use KPFM to investigate the effects of therapeutic agents at the subcellular level. For instance, KPFM was employed to examine HepG2 liver cancer cells treated with increasing concentrations of curcumin, revealing its unique capacity to simultaneously resolve mechanical stiffness and ESP at subcellular resolution (**Figure 11a,e**).[30] The analysis showed a biphasic change in the mechanical properties of nuclear and cytoplasmic regions, with an initial increase followed by a decline as curcumin concentration rose. Importantly, KPFM uncovered a striking rise in heterogeneity of the ESP, with a pronounced increase in low-potential zones.[30] These nanoscale signatures, detectable only through high-resolution KPFM, correlate with curcumin's well-established anti-proliferative effects.[180–182] and support its selective toxicity toward liver cancer cells.[183]

In a related work, KPFM was used to explore how oxidative stress influences the electronic properties of neuronal membranes. By mapping the ESP of PC12 cell plasma membranes exposed to various reactive oxygen species (ROS)—including H_2O_2, dopamine, Zn^{2+}, and PS micelles—KPFM revealed distinct shifts in electrostatic distribution patterns (Figure 11b).[29] These nanoscale potential maps highlight the sensitivity of membrane electrostatics to environmental and molecular stimuli. While the exact biochemical mechanisms underlying these changes remain to be elucidated, the ability of KPFM to capture such nuanced electrochemical perturbations reinforces its value as a frontline technique for probing cellular responses to oxidative stress.

To further explore the functional implications of membrane electrostatics in neuronal systems, Zhao et al.[31] applied KPFM to map the nanoscale ESP and capacitance gradients of distinct neuronal structures, including PC12 cells, hippocampal neurons, and dendritic spines (Figure 11c,d). Despite their structural differences, these cells exhibited remarkably similar capacitance gradients (19–23 zF nm^{-1}), suggesting a conserved capacity for charge storage. However, the ESP varied significantly: it was least negative in PC12 cells and became progressively more negative in hippocampal neurons and dendritic spines. This spatial gradient in surface charge points to a distinct electrochemical environment within dendritic spines, potentially optimizing them for signal transduction and synaptic plasticity. These findings

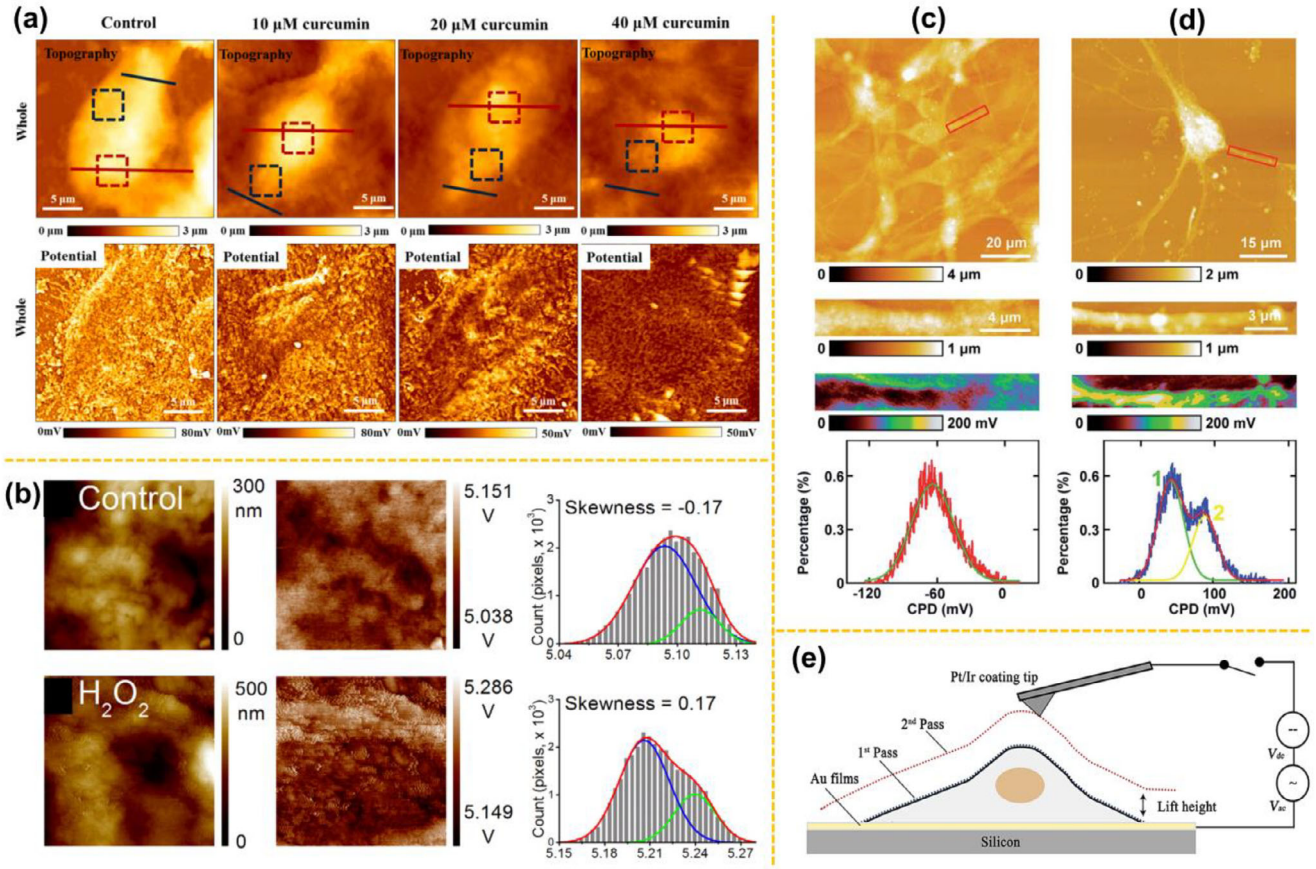

Figure 11. a) Topography and ESP maps of nuclear regions and cytoplasm regions on the HepG2 cells treated with various concentrations of curcumin (0, 10, 20, and 40 μM). Adapted with permission.[30] Copyright 2024, Elsevier. b) Oxidative stress caused a positive shift in skewness values. (a,b) illustrate AFM (left) and KPFM (middle) images of PC12 cells exposed to buffer (Control) and H_2O_2. Skewness was binned into 40 intervals and analyzed per cell (right column). The distributions were fitted with a two-peak Gaussian model (red line), with blue and green representing individual components. Adapted with permission.[29] Copyright 2012, PLOS One. Analysis of contact potential difference (CPD) in PC12 cells and hippocampal neurons: c) PC12 cell topography; close-up of the red-highlighted region in (c); associated CPD map and corresponding histogram of CPD values; d) hippocampal neuron topography; close-up of the red-highlighted region in (d); associated CPD map and corresponding histogram of CPD values. Adapted with permission.[31] Copyright 2019, The Royal Society of Chemistry. e) Schematic representation of KPFM measurements on various cell parts. Adapted with permission.[30] Copyright 2024, Elsevier.

reinforce the idea that nanoscale variations in membrane potential are closely linked to cellular function and further highlight KPFM's utility in revealing electrostatic signatures that may inform future studies of neuronal signalling and disease.

Overall, from case studies involving liver cancer cells and redox-perturbed neuronal models, KPFM has shown promise in revealing ESP heterogeneity, particularly in relation to drug-induced changes and membrane composition in cancer cells. However, its application in cancer diagnostics or screening remains in early stages. Challenges include measurement throughput, variability in cell morphology, and the influence of substrates or fixation methods. To move forward, future efforts should focus on standardizing measurement protocols, minimizing environmental artifacts, and exploring how ESP signatures correlate with well-established biochemical markers of cell malignancy. Integrating KPFM with high-throughput platforms or label-free biosensing technologies could also be promising strategies to enhance its relevance in applied cancer research.

8. Conclusion and Perspectives

KPFM is emerging as a transformative tool at the intersection of nanotechnology, surface science, and life sciences, offering an unprecedented window into the spatial and electrochemical complexity of biological systems. Its unique ability to resolve nanoscale ESP distribution with high sensitivity and spatial resolution, even under near-physiological conditions, has positioned KPFM as a key technique for investigating biomolecular interactions and biointerfaces. In this context, this review has outlined the rapidly evolving landscape of KPFM applications in bionanotechnology, encompassing diverse targets such as DNA hybridization, aptamer–protein binding, membrane dynamics, and fibril aggregation.

One of the most compelling aspects of KPFM lies in its adaptability. Its integration with diverse nanoscale materials provides a robust platform for studying functionalized biomolecules and advancing the seamless coupling of biological systems with nanostructured materials. However, despite its versatility, KPFM

is not without challenges. Background noise, surface defects, and contaminants can compromise the accuracy and reliability of ESP measurements.[184,185] To address these issues, recent advancements have focused on improving spatial resolution, measurement accuracy, and reproducibility. The implementation of nanoscale patterned substrates incorporating nanomaterials such as nanoparticles, nanowires, or 2D sheets has further enhanced sensitivity and specificity for molecular interaction detection while minimizing artificial measurement influences.

Still, performing reliable measurements in liquid environments and mitigating surface contamination in biological samples remain critical challenges that demand continued innovation.[64] To overcome these hurdles and fully realize the potential of KPFM in life sciences, concrete methodologies must be actively developed. In this direction, in situ AC-KPFM and OL-EPM, by avoiding DC bias feedback loops,[65,106] are enabling stable probing of local ESP distributions and facilitating the mapping of redox activity in biological assemblies under near-physiological conditions.

A further limitation—but also an exciting frontier—for KPFM in biological systems is its temporal resolution. Current scan speeds remain insufficient to capture rapid dynamic processes such as synaptic transmission,[186] vesicle trafficking,[187] or protein conformational transitions.[188] While AC-KPFM[64] and OL-EPM[106] provide a foundation for time-resolved measurements, further innovation is needed to precisely monitor fast biological events in real time.

We anticipate that these advancements will center around the development of multi-frequency KPFM, which enables simultaneous excitation and detection at multiple harmonics, thereby reducing acquisition time by capturing richer electrostatic information per scan. In parallel, AI-driven cantilever control[66] could dynamically optimize measurement parameters in real time to compensate for tip-sample instabilities and drift—both critical for achieving reliable, high-speed imaging. Advanced signal processing techniques will further enhance the extraction of weak, high-frequency electrostatic signals that encode transient behaviors. Complementing these hardware and analytical improvements, the integration of KPFM with high-speed AFM,[189,190] pump-probe modalities,[191] and correlative imaging techniques—such as super-resolution fluorescence microscopy,[192] Raman spectroscopy,[193] and single-molecule force spectroscopy—will provide multidimensional insights into ultra-fast bioelectrical processes.

In this context, the recently developed peak force infrared–KPFM (PFIR-KPFM) deserves special attention, as it enables simultaneous mapping of chemical composition, ESP, and mechanical properties with ≈10 nm spatial resolution in a single-pass scan.[196,197] By combining infrared nanoimaging and ESP detection within the same operational cycle, PFIR-KPFM overcomes longstanding challenges related to drift and spatial mismatch in multimodal SPM.[196] This integration holds particular promise for investigating complex biointerfaces—such as amyloid fibrils—by uncovering intricate correlations between local charge distribution, molecular conformation, and mechanical stiffness.[196] Similarly, infrared scattering-type scanning near-field optical microscopy (s-SNOM), when combined with KPFM, expands the capabilities of nanoscale optical–electrical imaging and has shown broad applicability in characterizing functional materials, including photovoltaics and phase-change media.[198,199] These hybrid approaches represent a promising frontier for the multimodal characterization of biointerfaces and bioelectronic devices, with strong potential to unravel nanoscale structure–function relationships in heterogeneous biological systems and soft matter. Finally, the development of bio-compatible probes, ultra-soft cantilevers,[194] and integrated microfluidic AFM systems[195] will further extend the applicability of KPFM to living systems and high-throughput environments.

In parallel with technological advances, theoretical modeling of the EDL, ionic screening, and tip-sample interactions in complex biological environments must continue to evolve in in situ KPFM. Current models, such as classical Poisson–Boltzmann approaches, often fall short in the presence of multivalent ions, charged macromolecules, or spatially confined environments like nanopores.[66] Coupling experimental KPFM data with molecular dynamics simulations and advanced electrochemical models may bridge this gap, providing a more comprehensive picture of nanoscale bioelectrical phenomena.

Moving beyond the challenges of fundamental research, the broader deployment of KPFM in practical biosensing, screening, and diagnostic platforms remains constrained by several operational limitations. These include slow scanning speeds, sensitivity to environmental drift, complexity of operation, and the lack of standardized, high-throughput instrumentation accessible to non-expert users.[66] Additionally, requirements for vibration isolation, stable conductive tips, and precise tip-sample control limit the potential for integration into portable or real-time sensing devices. Addressing these obstacles will require substantial progress in miniaturized AFM design, robust automated scanning routines, and AI-assisted signal processing. In addition, we envision that the development of scalable, multiplexed KPFM systems—coupled with microfluidic interfaces and integrated data interpretation frameworks—could ultimately transform KPFM from a specialized surface characterization technique into a practical and versatile tool for real-world applications in bionanotechnology.

Ultimately, the greatest potential of KPFM in biological research lies in progress along two complementary fronts: technological advancement and real-world applicability. Continued innovation will enhance KPFM's capacity to bridge spatial, temporal, and physico-chemical resolution, enabling deeper insights into complex biological processes that remain poorly understood. In parallel, the successful translation of KPFM into practical sensing and diagnostic platforms could unlock real-time, non-destructive, and label-free monitoring of disease progression—a critical capability for advancing both systems biology and precision medicine.

Acknowledgements

This work was financially supported by Delft University of Technology (TUDelft), the University of Barcelona, and ETH Zurich. M. P.-C acknowledges that the projects that gave rise to this work received the support of a fellowship from "la Caixa" Foundation (ID 100010434) with code LCF/BQ/PI24/12040015 and the María de Maeztu, project no. CEX2021-001202. JPL acknowledges the Generalitat de Catalunya (2021 SGR 00270) and the Agencia Estatal de Investigación (AEI) for the María de Maeztu, project no. CEX2021-001202-M. S.P., and J.P.-L. also acknowledge support

from the European Union's Horizon Europe Research and Innovation Programme under the EVA project (GA no: 101047081).

Conflict of Interest

The authors declare no conflict of interest.

Author Contributions

E.R and M.P.-C contributed equally to this work. The manuscript was written and revised through the contributions of all authors. All authors have given approval to the final version of the manuscript. E. R. and M.P.C. have an equal contribution.

Keywords

biofunctionalized surface, biotechnology, KPFM, nanoscience, surface potential

Received: June 5, 2025
Revised: August 6, 2025
Published online:

[1] A. C. Ahn, B. J. Gow, Ø. G. Martinsen, M. Zhao, A. J. Grodzinsky, I. D. Baikie, *Phys. Rev. E Stat. Nonlin. Soft Matter Phys.* **2012**, *85*, 061901.
[2] M. Salerno, S. Dante, *Materials* **2018**, *11*, 951.
[3] L.-Z. Cheong, W. Zhao, S. Song, C. Shen, *Acta Biomater.* **2019**, *99*, 33.
[4] N. Wu, M. Barahona, S. N. Yaliraki, *Curr. Opin. Struct. Biol.* **2024**, *84*, 102737.
[5] Y.-L. Ying, Y.-X. Hu, R. Gao, R.-J. Yu, Z. Gu, L. P. Lee, Y.-T. Long, *J. Am. Chem. Soc.* **2018**, *140*, 5385.
[6] R. Callender, R. B. Dyer, *Acc. Chem. Res.* **2015**, *48*, 407.
[7] A. K. Sinensky, A. M. Belcher, *Nat. Nanotechnol.* **2007**, *2*, 653.
[8] J. Park, J. Yang, G. Lee, C. Y. Lee, S. Na, S. W. Lee, S. Haam, Y.-M. Huh, D. S. Yoon, K. Eom, *ACS Nano* **2011**, *5*, 6981.
[9] B. Mallada, A. Gallardo, M. Lamanec, B. De La Torre, V. Špirko, P. Hobza, P. Jelinek, *Science* **2021**, *374*, 863.
[10] B. Mallada, M. Ondráček, M. Lamanec, A. Gallardo, A. Jiménez-Martín, B. de la Torre, P. Hobza, P. Jelínek, *Nat. Commun.* **2023**, *14*, 4954.
[11] D. Wu, P. Kaur, Z. M. Li, K. C. Bradford, H. Wang, D. A. Erie, *Mol. Cell* **2016**, *61*, 315.
[12] G. I. Livshits, J. Ghabboun, N. Borovok, A. B. Kotlyar, D. Porath, *Adv. Mater.* **2014**, *26*, 4981.
[13] H. Du, D. Li, Y. Wang, C. Wang, D. Zhang, Y.-l. Yang, C. Wang, *J. Phys. Chem. B* **2013**, *117*, 9895.
[14] T. Rakshit, R. Mukhopadhyay, *Langmuir* **2011**, *27*, 9681.
[15] E. A. D. Pia, Q. Chi, D. D. Jones, J. E. Macdonald, J. Ulstrup, M. Elliott, *Nano Lett.* **2011**, *11*, 176.
[16] S. Bera, J. Kolay, P. Pramanik, A. Bhattacharyya, R. Mukhopadhyay, *J. Mater. Chem. C* **2019**, *7*, 9038.
[17] G. Zhou, Y. Yao, Z. Lu, X. Yang, J. Han, G. Wang, X. Rao, P. Li, Q. Liu, Q. Song, *Nanotechnology* **2017**, *28*, 425202.
[18] V. Palermo, M. Palma, P. Samorì, *Adv. Mater.* **2006**, *18*, 145.
[19] A. Liscio, V. Palermo, P. Samorì, *Acc. Chem. Res.* **2010**, *43*, 541.
[20] E. Rahimi, A. Imani, D. Kim, M. Rahimi, L. Fedrizzi, A. Mol, E. Asselin, S. Pané, M. Lekka, *ACS Appl. Mater. Interfaces* **2024**, *16*, 53299.
[21] E. Rahimi, R. Offoiach, K. Baert, H. Terryn, L. Fedrizzi, M. Lekka, *J. Electrochem. Soc.* **2022**, *169*, 031507.
[22] V. Palermo, A. Liscio, M. Palma, M. Surin, R. Lazzaroni, P. Samorì, *Chem. Commun.* **2007**, *3311*, 3328.
[23] K. Nam, K. Eom, J. Yang, J. Park, G. Lee, K. Jang, H. Lee, S. W. Lee, D. S. Yoon, C. Y. Lee, *J. Mater. Chem.* **2012**, *22*, 23348.
[24] A. D. D. Stone, P. Mesquida, *Appl. Phys. Lett.* **2016**, *108*, 233702.
[25] D. Lee, H. Lee, G. Lee, I. Kim, S. W. Lee, W. Kim, S. W. Lee, J. H. Lee, J. Park, D. S. Yoon, *Nanotechnology* **2018**, *30*, 085501.
[26] K. Jang, J. Choi, C. Park, S. Na, *Biosens. Bioelectron.* **2017**, *87*, 222.
[27] M. Rufin, M. Nalbach, M. Rakuš, M. Fuchs, M. Poik, G. Schitter, P. J. Thurner, O. G. Andriotis, *Acta Biomater.* **2024**, *189*, 208.
[28] G. Lee, W. Lee, H. Lee, S. W. Lee, D. Sung Yoon, K. Eom, T. Kwon, *Appl. Phys. Lett.* **2012**, *101*, 043703.
[29] C.-C. Tsai, H.-H. Hung, C.-P. Liu, Y.-T. Chen, C.-Y. Pan, *PLoS One* **2012**, *7*, 33849.
[30] Z. Guo, Y. Meng, S. Zhou, J. Li, X. Li, R. Feng, Y. Zou, W. Liao, W. Wu, M. Xu, *J. Pharm. Biomed. Anal.* **2024**, *243*, 116107.
[31] W. Zhao, W. Cui, S. Xu, L.-Z. Cheong, D. Wang, C. Shen, *Nanoscale Adv.* **2019**, *1*, 537.
[32] H. Schmidt, S. Habicht, S. Feste, A.-D. Müller, O. G. Schmidt, *Appl. Surf. Sci.* **2013**, *281*, 24.
[33] H. Lee, W. Lee, J. H. Lee, D. S. Yoon, *J. Nanomater.* **2016**, *2016*, 4209130.
[34] J. Weaver, D. W. Abraham, *J. Vac. Sci. Technol. B Microelectron. process. phenom.* **1991**, *9*, 1559.
[35] M. Nonnenmacher, M. o'Boyle, H. K. Wickramasinghe, *Appl. Phys. Lett.* **1991**, *58*, 2921.
[36] E. G. Castanon, A. F. Scarioni, H. W. Schumacher, S. Spencer, R. Perry, J. A. Vicary, C. A. Clifford, H. Corte-León, *J. Phys. Commun.* **2020**, *4*, 095025.
[37] S. Sadewasser, T. Glatzel, *Kelvin probe force microscopy*, Springer, Berlin **2012**.
[38] W. Melitz, J. Shen, A. C. Kummel, S. Lee, *Surf. Sci. Rep.* **2011**, *66*, 1.
[39] A. Farokh Payam, A. Passian, *Sci. Adv.* **2023**, *9*, adg8292.
[40] E. Rahimi, A. Imani, M. Lekka, F. Andreatta, Y. Gonzalez-Garcia, J. M. C. Mol, E. Asselin, L. Fedrizzi, *Langmuir* **2022**, *38*, 10854.
[41] O. Cherniavskaya, L. Chen, V. Weng, L. Yuditsky, L. E. Brus, *J. Phys. Chem. B* **2003**, *107*, 1525.
[42] E. Rahimi, R. Offoiach, S. Hosseinpour, A. Davoodi, K. Baert, A. Lutz, H. Terryn, M. Lekka, L. Fedrizzi, *Appl. Surf. Sci.* **2021**, *563*, 150364.
[43] U. Zerweck, C. Loppacher, T. Otto, S. Grafström, L. M. Eng, *Phys. Rev. B* **2005**, *71*, 125424.
[44] C. Leung, D. Maradan, A. Kramer, S. Howorka, P. Mesquida, B. W. Hoogenboom, *Appl. Phys. Lett.* **2010**, *97*, 203703.
[45] C. Leung, H. Kinns, B. W. Hoogenboom, S. Howorka, P. Mesquida, *Nano Lett.* **2009**, *9*, 2769.
[46] D. S. Jakob, H. Wang, X. G. Xu, *ACS Nano* **2020**, *14*, 4839.
[47] A. Zahmatkeshsaredorahi, D. S. Jakob, X. G. Xu, *J. Phys. Chem. C* **2024**, *128*, 9813.
[48] A. Zahmatkeshsaredorahi, D. S. Jakob, H. Fang, Z. Fakhraai, X. G. Xu, *Nano Lett.* **2023**, *23*, 8953.
[49] F. Schulz, J. Ritala, O. Krejci, A. P. Seitsonen, A. S. Foster, P. Liljeroth, *ACS Nano* **2018**, *12*, 5274.
[50] E. Rahimi, R. Offoiach, S. Deng, X. Chen, S. Pané, L. Fedrizzi, M. Lekka, *Appl. Mater. Today* **2021**, *24*, 101135.
[51] I. Spajić, E. Rahimi, M. Lekka, R. Offoiach, L. Fedrizzi, I. Milošev, *J. Electrochem. Soc.* **2021**, *168*, 071510.
[52] E. Rahimi, D. Kim, R. Offoiach, R. Sanchis-Gual, X. Z. Chen, P. Taheri, Y. Gonzalez-Garcia, J. M. Mol, L. Fedrizzi, S. Pané, *Adv. Mater. Interfaces* **2023**, *10*, 2300558.
[53] J. L. Neff, P. Rahe, *Phys. Rev. B* **2015**, *91*, 085424.

[54] T. Glatzel, S. Sadewasser, R. Shikler, Y. Rosenwaks, M. C. Lux-Steiner, *Mater. Sci. Eng., B* **2003**, *102*, 138.
[55] C. Sommerhalter, T. W. Matthes, T. Glatzel, A. Jäger-Waldau, M. C. Lux-Steiner, *Appl. Phys. Lett.* **1999**, *75*, 286.
[56] E. M. Lanzoni, T. Gallet, C. Spindler, O. Ramírez, C. K. Boumenou, S. Siebentritt, A. Redinger, *Nano Energy* **2021**, *88*, 106270.
[57] M. N. Larsen, M. S. Peters, R. Lemos-Silva, D. A. Da Silva Filho, B. Jørgensen, O. Albrektsen, J. Kjelstrup-Hansen, *Org. Electron.* **2021**, *89*, 106060.
[58] M. Saint Jean, S. Hudlet, C. Guthmann, J. Berger, *Phys. Rev. B* **1997**, *56*, 15391.
[59] O. A. Castañeda-Uribe, R. Reifenberger, A. Raman, A. Avila, *ACS Nano* **2015**, *9*, 2938.
[60] F. Fuchs, F. Caffy, R. Demadrille, T. Mélin, B. Grévin, *ACS Nano* **2016**, *10*, 739.
[61] V. W. Bergmann, S. A. Weber, F. Javier Ramos, M. K. Nazeeruddin, M. Grätzel, D. Li, A. L. Domanski, I. Lieberwirth, S. Ahmad, R. Berger, *Nat. Commun.* **2014**, *5*, 5001.
[62] C. E. Kehayias, S. MacNaughton, S. Sonkusale, C. Staii, *Nanotechnology* **2013**, *24*, 245502.
[63] K.-i. Umeda, K. Kobayashi, N. Oyabu, Y. Hirata, K. Matsushige, H. Yamada, *J. Appl. Phys.* **2014**, *116*, 134307.
[64] T. Hackl, G. Schitter, P. Mesquida, *ACS Nano* **2022**, *16*, 17982.
[65] K. Honbo, S. Ogata, T. Kitagawa, T. Okamoto, N. Kobayashi, I. Sugimoto, S. Shima, A. Fukunaga, C. Takatoh, T. Fukuma, *ACS Nano* **2016**, *10*, 2575.
[66] L. Collins, J. I. Kilpatrick, S. V. Kalinin, B. J. Rodriguez, *Rep. Prog. Phys.* **2018**, *81*, 086101.
[67] A. Dominguez-Alfaro, N. Casado, M. Fernandez, A. Garcia-Esnaola, J. Calvo, D. Mantione, M. R. Calvo, A. L. Cortajarena, *Small* **2024**, *20*, 2307536.
[68] S. Berhanu, S. Majumder, T. Müntener, J. Whitehouse, C. Berner, A. K. Bera, A. Kang, B. Liang, N. Khan, B. Sankaran, *Science* **2024**, *385*, 282.
[69] N. L. Ing, M. Y. El-Naggar, A. I. Hochbaum, *J. Phys. Chem. B* **2018**, *122*, 10403.
[70] C. D. Bostick, S. Mukhopadhyay, I. Pecht, M. Sheves, D. Cahen, D. Lederman, *Rep. Prog. Phys.* **2018**, *81*, 026601.
[71] E. Rahimi, R. Offoiach, K. Baert, H. Terryn, M. Lekka, L. Fedrizzi, *Materialia* **2021**, *15*, 100988.
[72] C. Di Franco, M. Piscitelli, E. Macchia, C. Scandurra, M. Catacchio, L. Torsi, G. Scamarcio, *J. Mater. Chem. C* **2024**, *12*, 73.
[73] B. E. Feller, J. T. Kellis Jr., L. G. Cascão-Pereira, C. R. Robertson, C. W. Frank, *Langmuir* **2011**, *27*, 250.
[74] Q. Yang, B. Wang, Z. Zhang, D. Lou, J. Tan, L. Zhu, *RSC Adv.* **2017**, *7*, 38028.
[75] B. Poolman, J. J. Spitzer, J. M. Wood, *Biochim. Biophys. Acta, Biomembr.* **2004**, *1666*, 88.
[76] T. Yeung, S. Grinstein, *Immunol. Rev.* **2007**, *219*, 17.
[77] R. Roskoski, *Pharmacol. Res.* **2015**, *100*, 1.
[78] R. Kannaiyan, D. Mahadevan, *Expert Rev. Anticancer Ther.* **2018**, *18*, 1249.
[79] B. Bilanges, N. Torbett, B. Vanhaesebroeck, *Nat. Chem. Biol.* **2008**, *4*, 648.
[80] I. Melnikova, J. Golden, *Nat. Rev. Drug Discovery* **2004**, *3*, 993.
[81] P. Arosio, R. Ingrassia, P. Cavadini, *Biochim Biophys Acta* **2009**, *1790*, 589.
[82] J. Volatron, J. Kolosnjaj-Tabi, Y. Javed, Q. L. Vuong, Y. Gossuin, S. Neveu, N. Luciani, M. Hémadi, F. Carn, D. Alloyeau, *Sci. Rep.* **2017**, *7*, 40075.
[83] G. Liu, J. Gao, H. Ai, X. Chen, *Small* **2013**, *9*, 1533.
[84] T. Rakshit, S. Banerjee, S. Mishra, R. Mukhopadhyay, *Langmuir* **2013**, *29*, 12511.
[85] P. Balasubramanian, M. P. Prabhakaran, M. Sireesha, S. Ramakrishna, in *Collagen in Human Tissues: Structure, Function, and Biomedical Implications from a Tissue Engineering Perspective*, (Eds.: A. Abe, H.-H. Kausch, M. Möller, H. Pasch) Springer, Berlin, Heidelberg, **2013**, pp. 173–206.
[86] D. F. Holmes, Y. Lu, T. Starborg, K. E. Kadler, in *Current Topics in Developmental Biology*, (Eds.: E.S. Litscher, P.M. Wassarman), Academic Press, Cambridge, MA, USA **2018**, pp. 107–142.
[87] S. V. Plotnikov, A. M. Pasapera, B. Sabass, C. M. Waterman, *Cell* **2012**, *151*, 1513.
[88] O. G. Andriotis, S. Desissaire, P. J. Thurner, *ACS Nano* **2018**, *12*, 3671.
[89] D. Denning, J. I. Kilpatrick, E. Fukada, N. Zhang, S. Habelitz, A. Fertala, M. D. Gilchrist, Y. Zhang, S. A. M. Tofail, B. J. Rodriguez, *ACS Biomater. Sci. Eng.* **2017**, *3*, 929.
[90] J. Kwon, H. Cho, *ACS Biomater. Sci. Eng.* **2020**, *6*, 6680.
[91] A. Bazaid, S. M. Neumayer, A. Sorushanova, J. Guyonnet, D. Zeugolis, B. J. Rodriguez, *Biomed. Phys. Eng. Express* **2017**, *3*, 055004.
[92] J. Kwon, H. Cho, *Commun. Biol.* **2022**, *5*, 1229.
[93] Y. Zhang, Y. Wang, Z. Zhang, Z. Wang, C. Shao, M. Hannig, Z. Zhou, B. Fu, *Nanoscale Adv.* **2024**, *6*, 467.
[94] E. Gachon, P. Mesquida, *ACS Nano* **2021**, *15*, 9820.
[95] S. Bansode, U. Bashtanova, R. Li, J. Clark, K. H. Müller, A. Puszkarska, I. Goldberga, H. H. Chetwood, D. G. Reid, L. J. Colwell, *Sci. Rep.* **2020**, *10*, 3397.
[96] C. Di Franco, E. Macchia, M. Catacchio, M. Caputo, C. Scandurra, L. Sarcina, P. Bollella, A. Tricase, M. Innocenti, R. Funari, M. Piscitelli, G. Scamarcio, L. Torsi, *Adv. Sci.* **2025**, *12*, 2412347.
[97] E. Macchia, F. Torricelli, M. Caputo, L. Sarcina, C. Scandurra, P. Bollella, M. Catacchio, M. Piscitelli, C. Di Franco, G. Scamarcio, *Adv. Mater.* **2024**, *36*, 2309705.
[98] T. Kwon, J. Park, G. Lee, K. Nam, Y.-M. Huh, S.-W. Lee, J. Yang, C. Y. Lee, K. Eom, *J. Phys. Chem. Lett.* **2013**, *4*, 1126.
[99] S. Emaminejad, M. Javanmard, C. Gupta, S. Chang, R. W. Davis, R. T. Howe, *Proc. Natl. Acad. Sci.* **2015**, *112*, 1995.
[100] Y. Han, Y. Cao, J. Zhou, Y. Yao, X. Wu, S. Bolisetty, M. Diener, S. Handschin, C. Lu, R. Mezzenga, *Adv. Sci.* **2023**, *10*, 2206867.
[101] P. Salahuddin, M. T. Fatima, V. N. Uversky, R. H. Khan, Z. Islam, M. Furkan, *Int. J. Biol. Macromol.* **2021**, *190*, 44.
[102] T. Hayashida, T. Kawashima, D. Nii, K. Ozasa, K. Umemura, *Chem. Lett.* **2013**, *42*, 666.
[103] M. Calamai, J. R. Kumita, J. Mifsud, C. Parrini, M. Ramazzotti, G. Ramponi, N. Taddei, F. Chiti, C. M. Dobson, *Biochemistry* **2006**, *45*, 12806.
[104] W. Lee, H. Jung, M. Son, H. Lee, T. J. Kwak, G. Lee, C. H. Kim, S. W. Lee, D. S. Yoon, *RSC Adv.* **2014**, *4*, 56561.
[105] Y. Yoshiike, T. Akagi, A. Takashima, *Biochemistry* **2007**, *46*, 9805.
[106] V. V. S. Pillai, P. Kumari, S. Kolagatla, V. Garcia Sakai, S. Rudić, B. J. Rodriguez, M. Rubini, K. M. Tych, A. Benedetto, *J. Phys. Chem. Lett.* **2022**, *13*, 7058.
[107] W. Qiang, M. K. Kengewerere, J. M. Kenyaga, *J. Phys. Chem. B* **2024**, *128*, 5667.
[108] Y. Liu, B. Ren, Y. Zhang, Y. Sun, Y. Chang, G. Liang, L. Xu, J. Zheng, *Biochim. Biophys. Acta, Biomembr.* **2018**, *1860*, 1906.
[109] J.-C. Rochet, *Expert Rev. Mol. Med.* **2007**, *9*, 1.
[110] F. M. Menger, C. Littau, *J. Am. Chem. Soc.* **1991**, *113*, 1451.
[111] A. J. Kirby, P. Camilleri, J. B. Engberts, M. C. Feiters, R. J. Nolte, O. Söderman, M. Bergsma, P. C. Bell, M. L. Fielden, C. L. García Rodríguez, *Angew. Chem., Int. Ed.* **2003**, *42*, 1448.
[112] T. Ahmed, A. O. Kamel, S. D. Wettig, *Nanomedicine* **2016**, *11*, 289.
[113] P. Yang, J. Singh, S. Wettig, M. Foldvari, R. E. Verrall, I. Badea, *Eur. J. Pharm. Biopharm.* **2010**, *75*, 311.

[114] A. M. Cardoso, C. M. Morais, A. R. Cruz, A. L. Cardoso, S. G. Silva, M. L. do Vale, E. F. Marques, M. C. Pedroso de Lima, A.I.S. Jurado, *Mol. Pharmaceutics* **2015**, *12*, 716.
[115] Z. Lu, G. Zongjie, Z. Qianyu, L. Xueyan, W. Kexin, C. Baoyan, T. Ran, R. Fang, H. Hui, C. Huali, *Eur. J. Pharm. Biopharm.* **2023**, *182*, 92.
[116] E. Silva, U. Andrade, K. de Oliveira, A. Teixeira, M. Rocha, *Phys. Rev. E* **2020**, *102*, 032401.
[117] M. Akram, H. Lal, *Bioorg. Chem.* **2022**, *119*, 105555.
[118] E. Ojeda, G. Puras, M. Agirre, J. Zarate, S. Grijalvo, R. Eritja, G. Martinez-Navarrete, C. Soto-Sánchez, A. Díaz-Tahoces, M. Aviles-Trigueros, *Biomaterials* **2016**, *77*, 267.
[119] B. Ma, S. Zhang, H. Jiang, B. Zhao, H. Lv, *J. Controlled Release* **2007**, *123*, 184.
[120] A. Michanek, M. Yanez, H. Wacklin, A. Hughes, T. Nylander, E. Sparr, *Langmuir* **2012**, *28*, 9621.
[121] F. E. Ala'a, M. F. Paige, *J. Colloid Interface Sci.* **2012**, *380*, 105.
[122] F. Hane, B. Moores, M. Amrein, Z. Leonenko, *Ultramicroscopy* **2009**, *109*, 968.
[123] E. Finot, Y. Leonenko, B. Moores, L. Eng, M. Amrein, Z. Leonenko, *Langmuir* **2010**, *26*, 1929.
[124] M. Martínez-Negro, A. Guerrero-Martinez, L. García-Río, O.s. Domènech, E. Aicart, C. T. de Ilarduya, E. Junquera, *ACS Omega* **2018**, *3*, 208.
[125] A. L. Barrán-Berdón, B.n. Yélamos, L. García-Río, O.s. Domènech, E. Aicart, E. Junquera, *ACS Appl. Mater. Interfaces* **2015**, *7*, 14404.
[126] R. D. Henderson, C. T. Filice, S. Wettig, Z. Leonenko, *Soft Matter* **2021**, *17*, 826.
[127] B. Moores, F. Hane, L. Eng, Z. Leonenko, *Ultramicroscopy* **2010**, *110*, 708.
[128] R. D. Henderson, N. Mei, Y. Xu, R. Gaikwad, S. Wettig, Z. Leonenko, *Nanomaterials* **2024**, *14*, 572.
[129] J. L. Richens, J. S. Lane, J. P. Bramble, P. O'Shea, *Biochimica et Biophysica Acta (BBA)-Biomembranes* **2015**, *1848*, 1828.
[130] A. Whited, A. Johs, *Chem. Phys. Lipids* **2015**, *192*, 51.
[131] P. Gao, Y. Cai, *Anal. Bioanal. Chem.* **2009**, *394*, 207.
[132] E. Drolle, W. Bennett, K. Hammond, E. Lyman, M. Karttunen, Z. Leonenko, *Soft Matter* **2017**, *13*, 355.
[133] E. Drolle, R. M. Gaikwad, Z. Leonenko, *Biophys. J.* **2012**, *103*, L27.
[134] W.-C. Lin, C. D. Blanchette, T. V. Ratto, M. L. Longo, *Biophys. J.* **2006**, *90*, 228.
[135] S. Garcia-Manyes, F. Sanz, *Biochim. Biophys. Acta, Biomembr.* **2010**, *1798*, 741.
[136] M. E. Davis, J. A. McCammon, *Chem. Rev.* **1990**, *90*, 509.
[137] M. J. Packer, M. P. Dauncey, C. A. Hunter, *J. Mol. Biol.* **2000**, *295*, 71.
[138] S. Hormeno, M. Penedo, C. V. Manzano, M. Luna, *Nanotechnology* **2013**, *24*, 395701.
[139] A. Cerreta, D. Vobornik, G. Di Santo, S. Tobenas, L. Alonso-Sarduy, J. Adamcik, G. Dietler, *J. Mol. Recognit.* **2012**, *25*, 486.
[140] L. Nony, R. Boisgard, J.-P. Aimé, *Biomacromolecules* **2001**, *2*, 827.
[141] J. Park, S. Lee, K. Jang, S. Na, *Biosens. Bioelectron.* **2014**, *60*, 299.
[142] J. Xu, R. Jiang, Y. Feng, Z. Liu, J. Huang, C. Ma, K. Wang, *Coord. Chem. Rev.* **2022**, *459*, 214453.
[143] B. Jash, J. Müller, *Chem. Eur. J.* **2017**, *23*, 17166.
[144] P. Scharf, J. Müller, *ChemPlusChem* **2013**, *78*, 20.
[145] B. Jash, J. Neugebauer, J. Müller, *Inorg. Chim. Acta* **2016**, *452*, 181.
[146] J. Müller, *Coord. Chem. Rev.* **2019**, *393*, 37.
[147] A. Ono, S. Cao, H. Togashi, M. Tashiro, T. Fujimoto, T. Machinami, S. Oda, Y. Miyake, I. Okamoto, Y. Tanaka, *Chem. Commun.* **2008**, 4825.
[148] C. Bardehle, J. Müller, *Chem. Eur. J.* **2025**, *31*, 202404332.
[149] M. Saidur, A. A. Aziz, W. Basirun, *Biosens. Bioelectron.* **2017**, *90*, 125.
[150] Y. Zhou, L. Tang, G. Zeng, C. Zhang, Y. Zhang, X. Xie, *Sens. Actuators, B* **2016**, *223*, 280.
[151] L. M. Zanoli, R. D'Agata, G. Spoto, *Anal. Bioanal. Chem.* **2012**, *402*, 1759.
[152] S. Hu, P.-J. J. Huang, J. Wang, J. Liu, *Anal. Chem.* **2020**, *92*, 13354.
[153] J. Deka, A. Mojumdar, P. Parisse, S. Onesti, L. Casalis, *Sci. Rep.* **2017**, *7*, 44358.
[154] X. Lin, C. Li, C. He, Y. Zhou, Z. Wang, N. Duan, S. Wu, *ACS Appl. Nano Mater.* **2021**, *4*, 8231.
[155] Z. Skeete, H.-W. Cheng, J. Li, C. Salazar, W. Sun, Q. M. Ngo, L. Lin, J. Luo, C.-J. Zhong, *J. Phys. Chem. C* **2017**, *121*, 15767.
[156] H. Lee, S. W. Lee, G. Lee, W. Lee, J. H. Lee, K. S. Hwang, J. Yang, S. W. Lee, D. S. Yoon, *Nanoscale* **2016**, *8*, 13537.
[157] A. Merkoçi, *Biosens. Bioelectron.* **2010**, *26*, 1164.
[158] X. Li, T. Wu, *Chem. Eng. J.* **2024**, *482*, 149112.
[159] H. Lee, S. W. Lee, G. Lee, W. Lee, K. Nam, J. H. Lee, K. S. Hwang, J. Yang, H. Lee, S. Kim, *Nanoscale* **2018**, *10*, 538.
[160] M. K. McConechy, A. Talhouk, H. H. Li-Chang, S. Leung, D. G. Huntsman, C. B. Gilks, J. N. McAlpine, *Gynecol. Oncol.* **2015**, *137*, 306.
[161] M. J. Garnett, E. J. Edelman, S. J. Heidorn, C. D. Greenman, A. Dastur, K. W. Lau, P. Greninger, I. R. Thompson, X. Luo, J. Soares, Q. Liu, F. Iorio, D. Surdez, L. Chen, R. J. Milano, G. R. Bignell, A. T. Tam, H. Davies, J. A. Stevenson, S. Barthorpe, S. R. Lutz, F. Kogera, K. Lawrence, A. McLaren-Douglas, X. Mitropoulos, T. Mironenko, H. Thi, L. Richardson, W. Zhou, F. Jewitt, et al., *Nature* **2012**, *483*, 570.
[162] P. Miao, K. Han, B. Wang, G. Luo, P. Wang, M. Chen, Y. Tang, *Sci. Rep.* **2015**, *5*, 9161.
[163] P. AshaRani, G. Low Kah Mun, M. P. Hande, S. Valiyaveettil, *ACS Nano* **2009**, *3*, 279.
[164] X. Guo, A. A. Gorodetsky, J. Hone, J. K. Barton, C. Nuckolls, *Nat. Nanotechnol.* **2008**, *3*, 163.
[165] Z. Cohen, R. M. Williams, *ACS Nano* **2024**, *12*, 35164.
[166] R. Acharya, T. V. Patil, S. D. Dutta, J. Lee, K. Ganguly, H. Kim, A. Randhawa, K. T. Lim, *Adv. Mater. Technol.* **2024**, *9*, 2400279.
[167] H. M. Dewey, A. Lamb, J. Budhathoki-Uprety, *Nanoscale* **2024**, *16*, 1634.
[168] J. H. K. Rozenfeld, T. R. Oliveira, M. T. Lamy, A. M. Carmona-Ribeiro, *Biochim. Biophys. Acta, Biomembr.* **2011**, *1808*, 649.
[169] D. A. Ammendolia, W. M. Bement, J. H. Brumell, *BMC Biol.* **2021**, *19*, 71.
[170] A. Horn, J. K. Jaiswal, in *Current Topics in Membranes*, (Ed.: L.O. Andrade), Academic Press, Cambridge, MA, USA **2019**, pp. 67–98.
[171] G. R. Dubyak, *Adv. Physiol. Educ* **2004**, *28*, 143.
[172] R. Capone, H. Jang, S. A. Kotler, L. Connelly, F. Teran Arce, S. Ramachandran, B. L. Kagan, R. Nussinov, R. Lal, *J. Chem. Theory Comput.* **2012**, *8*, 1143.
[173] V. Fisi, A. Miseta, T. Nagy, *Oxid. Med. Cell. Longev.* **2017**, *2017*, 1308692.
[174] P. A. Leventis, S. Grinstein, *Annu. Rev. Biophys.* **2010**, *39*, 407.
[175] F. Neemann, S. Rosenberger, B. Jefferson, E. J. McAdam, *J. Membr. Sci.* **2013**, *446*, 310.
[176] H. Yuan, C. Guo, L. Liu, L. Zhao, Y. Zhang, T. Yin, H. He, J. Gou, B. Pan, X. Tang, *Carbohydr. Polym.* **2023**, *312*, 120838.
[177] C.-X. Li, Y.-L. Jing, Y.-K. Xie, *Brain Res.* **2007**, *1139*, 201.
[178] O. M. Shatnyeva, A. V. Kubarenko, C. E. Weber, A. Pappa, R. Schwartz-Albiez, A. N. Weber, P. H. Krammer, I. N. Lavrik, *PLoS One* **2011**, *6*, 19927.
[179] D. Li, Y. Wang, H. Du, S. Xu, Z. Li, Y. Yang, C. Wang, *Nanomaterials* **2016**, *6*, 197.
[180] J. Ma, B. Fang, F. Zeng, H. Pang, J. Zhang, Y. Shi, X. Wu, L. Cheng, C. Ma, J. Xia, *Toxicol. Lett.* **2014**, *231*, 82.
[181] A. Chen, J. Xu, A. Johnson, *Oncogene* **2006**, *25*, 278.
[182] Y. Liu, Y. Liu, X. Sun, Y. Wang, C. Du, J. Bai, *Mater. Today Bio.* **2024**, *24*, 100903.

[183] X. Liu, X. Miao, S. Bo, X. Deng, Z. Zhang, Y. Zheng, *J. Drug Deliv. Sci. Technol.* **2024**, *91*, 105237.
[184] D. J. Ellison, B. Lee, V. Podzorov, C. D. Frisbie, *Adv. Mater.* **2011**, *23*, 502.
[185] H. Diesinger, D. Deresmes, J. P. Nys, T. Mélin, *Ultramicroscopy* **2010**, *110*, 162.
[186] I. Park, H. J. Kim, J. Shin, Y. J. Jung, D. Lee, J.-s. Lim, J. M. Park, J. W. Park, J.-H. Kim, *Adv. Sci.* **2024**, *11*, 2306630.
[187] A. Ridolfi, M. Brucale, C. Montis, L. Caselli, L. Paolini, A. Borup, A. T. Boysen, F. Loria, M. J. C. van Herwijnen, M. Kleinjan, P. Nejsum, N. Zarovni, M. H. M. Wauben, D. Berti, P. Bergese, F. Valle, *Anal. Chem.* **2020**, *92*, 10274.
[188] Y. He, M. Lu, J. Cao, H. P. Lu, *ACS Nano* **2012**, *6*, 1221.
[189] T. Ando, N. Kodera, E. Takai, D. Maruyama, K. Saito, A. Toda, *Proc. Natl. Acad. Sci.* **2001**, *98*, 12468.
[190] N. Kodera, D. Yamamoto, R. Ishikawa, T. Ando, *Nature* **2010**, *468*, 72.
[191] Z. Schumacher, A. Spielhofer, Y. Miyahara, P. Grutter, *Appl. Phys. Lett.* **2017**, *110*, 053111.
[192] A. I. Gómez-Varela, D. R. Stamov, A. Miranda, R. Alves, C. Barata-Antunes, D. Dambournet, D. G. Drubin, S. Paiva, P. A. A. De Beule, *Sci. Rep.* **2020**, *10*, 1122.
[193] C. S. Sweetenham, M. Larraona-Puy, I. Notingher, *Appl. Spectrosc.* **2011**, *65*, 1387.
[194] F. Yu, J. Liu, S. Yu, Z. Yang, Y. Pan, N. Gao, Q. Zou, J. Jeon, in *2015 Transducers-2015 18th Int. Conf. on Solid-State Sensors, Actuators and Microsystems (TRANSDUCERS)*, IEEE, Anchorage, AK, USA **2015**, pp. 2260-2263.
[195] Y. Qiu, C.-C. Chien, B. Maroulis, J. Bei, A. Gaitas, B. Gong, *J. Cell. Physiol.* **2022**, *237*, 3222.
[196] D. S. Jakob, H. Wang, G. Zeng, D. E. Otzen, Y. Yan, X. G. Xu, *Angew. Chem., Int. Ed.* **2020**, *59*, 16083.
[197] L. Wang, H. Wang, X. G. Xu, *Chem. Soc. Rev.* **2022**, *51*, 5268.
[198] T.-X. Qin, E.-M. You, M.-X. Zhang, P. Zheng, X.-F. Huang, S.-Y. Ding, B.-W. Mao, Z.-Q. Tian, *Light: Science & Applications* **2021**, *10*, 84.
[199] J. Barnett, L. Wehmeier, A. Heßler, M. Lewin, J. Pries, M. Wuttig, J. M. Klopf, S. C. Kehr, L. M. Eng, T. Taubner, *Nano Lett.* **2021**, *21*, 9012.
[200] E. Drolle, W. Ngo, Z. Leonenko, L. Subbaraman, L. Jones, *Transl. Vis. Sci. Technol.* **2020**, *9*, 41.
[201] W. Lee, H. Lee, Y. Choi, K. S. Hwang, S. W. Lee, G. Lee, D. S. Yoon, *Macromol. Res.* **2017**, *25*, 1187.
[202] P. Mesquida, D. Kohl, O. G. Andriotis, P. J. Thurner, M. Duer, S. Bansode, G. Schitter, *Sci. Rep.* **2018**, *8*, 10126.

Ehsan Rahimi earned his Ph.D. in Environmental and Energy Engineering (2021, University of Udine, Italy), where he investigated localized degradation mechanisms in micro/nanoscale biomedical devices and soft biointerfaces using advanced electrochemical and high-resolution AFM/KPFM techniques. As part of his Marie Curie fellowship, he conducted research at the Multi-Scale Robotics Lab at ETH Zürich (2019), focusing on the biodegradation of micro/nanorobotic platforms. Since 2022, he has been a postdoctoral researcher at Delft University of Technology in Corrosion Technology and Electrochemistry group, specializing in advanced electrochemical techniques and nanoscale electronic property characterization via AFM/KPFM for biomaterials, functional coatings, and complex electrochemical interfaces.

Mario Palacios-Corella is a Junior Leader Fellow of the "La Caixa" Foundation at the University of Barcelona. He earned his PhD in Nanoscience and Nanotechnology from the University of Valencia in 2021. Since the early stages of his PhD, his research has included the synthesis, characterization and application porous and nonporous coordination polymers in diverse fields such as magnetism, energy storage, biomedicine, and small-scale robotics.

Arjan Mol is Professor Corrosion Technology and Electrochemistry at Delft University of Technology, The Netherlands. His research focuses on (i) local electrochemical analysis of corrosion mechanisms, (ii) interfacial bonding of organic coatings on metal surfaces and (iii) active protective and self-healing coatings. As from 2017, he is editor-in-chief of Elsevier's *Corrosion Science*. He served as Chair of the Scientific and Technology Advisory Committee, Vice-President, President and Past President of the European Federation of Corrosion in the period 2014-2022. In 2022 Arjan has received the European Corrosion Medal. In 2023 he was inaugurated as Fellow of the Netherlands Academy of Engineering.

Salvador Pané is a professor of materials for robotics and codirector of the Multi-Scale Robotics Lab (MSRL) at the ETH Zürich. He received his Ph.D. in chemistry from the University of Barcelona in 2008 and subsequently joined MSRL as a postdoctoral researcher in August 2008. He has been awarded the highly competitive ERC-Starting Grant (StG) and ERC Consolidator Grant (CoG) in 2012 and 2017, respectively. Since 2023, he is elected member of the Institut d'Estudis Catalans in the section of Science and Technology. His interests lie in bridging materials science, chemistry, and electrochemistry with small-scale robotics for various applications.

Josep Puigmartí-Luis is an ICREA Research Professor, a full professor, at University of Barcelona, where he heads ChemInFlow group. He earned his Ph.D. (ICMAB-CSIC) in 2008 and held an ETH Zürich Fellowship before founding an independent program that couples microfluidic technologies with chemistry and materials science. His work pioneered microfluidic reaction-diffusion control and simulated microgravity conditions inside microfluidic platforms to direct growth, shape, and properties of functional crystalline materials. His distinctions include Premi Antoni de Martí i Franquès de Ciències Químiques, St. Jordi Award, and IEEE 3M-NANO Rising Star Award in 2023; he was also a recipient of an ERC Starting Grant.